Development and Study of Hyperdamping Protective Material Systems for Shock Mitigation

Undergraduate Honors Thesis

Presented in Partial Fulfillment of the Requirements for Graduation with Distinction
in the Department of Mechanical and Aerospace Engineering of The Ohio State University

By

Sansriti Saxena

Undergraduate Program in Mechanical Engineering

The Ohio State University

April 2017

Thesis Committee:
Ryan L. Harne, Advisor
Shaurya Prakash

ABSTRACT

Helmets are used as personal protective equipment in a large variety of occupational and recreational activities. Despite the widespread use of helmets, concussions and traumatic brain injuries are still common due to ineffective diffusion and damping of the shock energies caused by impact events. Conventional foam liners for helmet designs require large quantities of stiff, deformable foam for shock absorption, increasing weight, and yet not providing adequate protection required to prevent head-related injuries. Hyperdamping materials are lightweight, elastomer materials able to absorb significant vibration and wave energy by harnessing principles from mechanics of beams for the material design. This research investigates the suitability for hyperdamping material systems to provide shock absorption properties without the conventional reliance of large quantities of energy-damping mass. Through the use of constrained arrays of elastomer beams, the development of hyperdamping protective materials for helmet design leads to substantial impact energy absorption with reduction in weight when compared to the host material itself. These new material designs are assessed through finite element analysis to gain an understanding of key design parameters and determine geometries suggesting promise to be explored in the laboratory. Experimentation then explores the practical aspects of attenuating shock and system acceleration due a variety of impulsive forces in two types of shock mitigation contexts. The first experimental context evaluates force reduction through the specimens according to significance of constraint. The second experimental context considers the relationship between impact force and system acceleration according to the change in constraint. Results of the experiments indicate that hyperdamping protective material systems provide significant reduction in force and acceleration with up to 40% reduction in mass compared to control specimens composed of the solid elastomer material. The results of this research demonstrate the viability of hyperdamping protective material systems as shock absorbers to be used in numerous shock mitigation applications, including helmets.

ACKNOWLEDGEMENTS

I want to thank my advisor, Dr. Harne, for his support, guidance, and endless enthusiasm for the work. I would never have succeeded with this research project without his encouragement and trust in my ability as an engineer.

I would also like to thank Dr. Shaurya Prakash for his time and dedication as my committee member.

All related experiments in this research are conducted in the Laboratory of Sound and Vibration Research (LSVR) that is directed by Dr. Harne.

TABLE OF CONTENTS

LIST OF FIGURES

LIST OF TABLES

1 INTRODUCTION

1.1 Background on materials and structures to protect against head injury

Personal protective equipment (PPE) is required in numerous industries and activities. Specifically, helmets have critical safety roles in sport and industrial operations, from piloting helicopters to biking to construction, where users are protected from shocks resulting from projectiles and other impact forces upon the head, decreasing risk of traumatic brain injury (TBI). Concussions are the most common type of TBI, caused by trauma on the brain from impact or sudden movement which stretches blood vessels in the brain and can cause damage to cranial nerves [1]. Despite the capability for helmets to inhibit severe shock transmission, approximately 300,000 sports-related concussions occur in the United States annually because the shock energies are ineffectually attenuated during the transmission from helmet to the head [2]. The average football player, for example, receives 103 *g*'s upon impact during a game [3]. One study conducted found that 60% of industry-related TBI resulted in death or disability [4]. Although severe and moderate TBI are highly dangerous, mild TBI is at least 10 times more common. Additionally, approximately 225,000 new patients each year show long-term impairment from mild TBI [5]. Thus, there is a significant demand for helmets with exceptional energy damping performance to reduce these incidences that affect people of all ages.

Several studies have been conducted on the minimum thresholds of force an acceleration on the brain to induce concussion in humans. The data varies for each study, with one report indicating that the human face and cranium can withstand impact induce accelerations in excess of 300 *g*'s [6] while another study concludes that a theoretical threshold of 70 to 75 *g* is tolerated prior to concussion [7]. Yet, minimum thresholds for concussions can oversimplify the effects of impact forces upon the brain and skull since impact force, angular and linear acceleration, location of impact, deceleration time, and prior concussion/head injury [8] [9] all affect the likelihood of concussion. As one study finds, impacts of less than 80 *g* can lead to concussion while impacts above 100 *g* do not always lead to concussion [10]. Therefore, it is important to design shock absorbers able to mitigate across a range of impact forces such that risk of concussion and TBI is lessened for every impact scenario.

Although helmet designs vary by use, most consist of a rigid outer shell to prevent penetration and distribute force over a large area and a crushable liner to attenuate and distribute force over the head [6]. Currently, most helmet designs use foam and/or elastomer lining inside the helmet in order to absorb impact forces. Expanded polystyrene (EPS) foam is one such common inner liner [11]. The stiff nature of EPS, however, leads to issues of helmet roll-off where the foam insufficiently conforms to the contour of the user's skull and therefore comes off easily. Additional, more resilient foam pads are required in the design in order to negate the roll-off [11]. These additional pads add to the weight of the helmet design. It is also possible that due to the stiffness of the foam, a certain force must be met before the foam begins absorbing the impact [12], allowing impacts below these minimum forces to be absorbed by the skull instead.

There are several shock absorber designs for helmets that use protective material concepts more advanced than simple foam liners. One of these designs is the Xenith Helmet [13], which uses pneumatic shock

absorbers. The design involves pucks filled with air that compress and vent on impact to absorb energy. Another design by Vicis [14] uses vertical struts and foam liner in combination with a softer outer shell. The vertical struts slow down impact forces by bending and buckling upon impact. Another design comes from 6D Helmets [15], a company that designed an elastomeric isolation damper. The dampers are an hourglass shape that allows both ends to move and rotate independently from one another. 6D Helmet designs use arrays of elastomeric isolation dampers with EPS foam on both ends to absorb impact energy. The Xenith and Vicis helmet designs can be seen in Figure 1. While these designs do increase damping from traditional helmet liners, they do not tackle issues related to weight and volume of helmet design and still often require large amounts of foam.

Figure 1: The Xenith [13] and Vicis [14] helmet designs

1.2 Review of previous research

The research of protective material systems is not new. Such material systems have often been realized using structures of repeating cells engineered to achieve extreme mechanical properties [16]. Many studies have been conducted on material properties and design involving the principles of geometry. These studies show the significance of protective material systems in energy absorbing and wave attenuating applications, such as helmet shock absorbers

Shan et. al. [17] considers the energy absorption of elastomer beams in deformed and undeformed states for use in creating energy-trapping, multistable, architected materials. The study finds that elastomer structures could absorb larger amounts of energy when under conditions of strain as the energy entering a system under load becomes trapped as elastic deformation of bistable elastic beams. Using the energy-trapping capability of tilted, elastic beams, Shan et. al. is able to develop several fully elastic and reusable energy-trapping architected materials. The top of Figure 2 shows the developed architected materials under deformation.

Programmable mechanical metamaterials [18] use a lattice of differently sized holes, or void patterns, to program the response of the structure based on confinement. The study finds that the programmable metamaterial, based on external constraints and loading force, can lead to large energy damping.

Rafsanjani et. al. [16] studies a mechanical metamaterial with a periodic arrangement of snapping units with tunable tensile behavior. In this design of curved parallel beams, a programmable mechanical response is achieved by triggering snap-through buckling and causing the metamaterial to exhibit a pattern switch in tension. The design allows for several multistable states until a full extension of due to tension is reached. The energy dissipation occurs due to the snap-through phenomenon, which increases damping of the structure. The bottom of Figure 2 displays the multistability of the metamaterial.

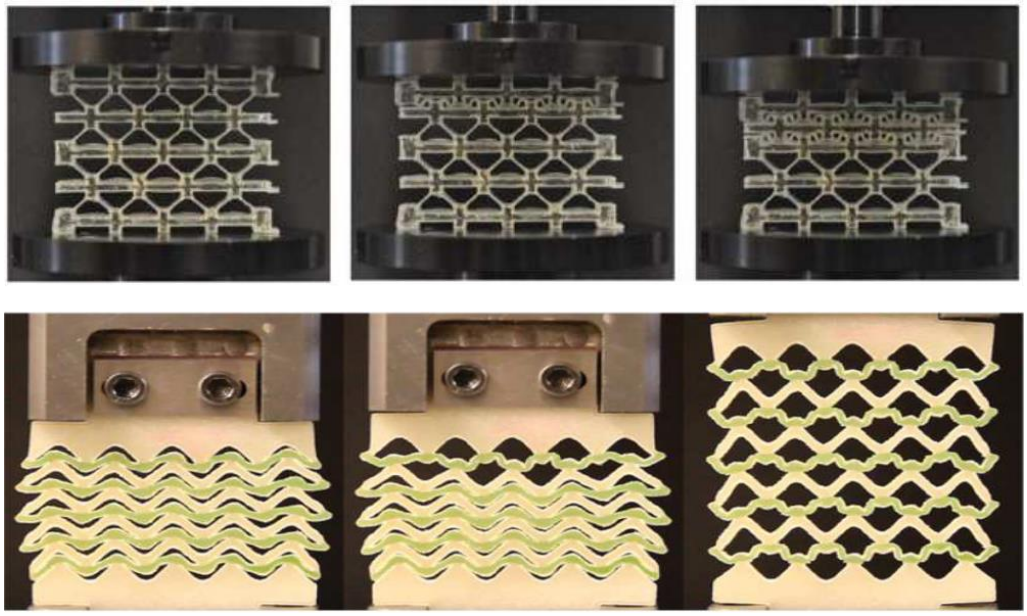

Figure 2: Examples of material systems. Top: multistable, architected materials [17]. Bottom: tunable, multistable metamaterials [16]

Hyperdamping material systems [19] are specific in that the energy dissipation of the metamaterial is a consequence of eliminating the fundamental stiffness contributions within the material system. They are lightweight, elastomer materials able to absorb significant vibration and wave energy by harnessing principles from mechanics of beams for the material design. Hyperdamping material systems use arrays of beams in compressed geometries to absorb energy. The compression of the geometry causes a constraint on the system, which leads to energy dissipation through the nullification of the natural frequency [19]. The fundamental modal damping ratio is inversely proportional to the natural frequency, as seen in Equation 1. Therefore, as the natural frequency goes to zero from the compression, the damping increases substantially in response.

$$\zeta = \frac{c}{2m\omega_n} \tag{1}$$

The use of hyperdamping material systems in helmet design could provide the necessary increase in energy absorption while reducing the required amount of padding and decreasing overall risk of brain injury.

1.3 Research goal

There are several issues to be addressed with current helmet designs, namely the insufficient force reduction and energy absorption of helmet liners upon impact and the unnecessary weight and volume from additional resilient foam pads. One study on the standards of safety helmets [20] suggests that there is an important demand for a more comfortable and acceptable helmet, meaning a significant reduction in weight and volume within the design while maintaining or increasing shock absorption. One possible solution to these issues is the integration of hyperdamping material systems into helmet designs.

The goal of this research is to investigate the use of hyperdamping protective material systems to mitigate and dampen shock energies. Such efforts will provide key preliminary information on the effectiveness of hyperdamping material systems to potentially be used in future helmet or headgear applications. While there is considerable research to show the vibration absorption of metamaterials, there is a specific need to show that hyperdamping material systems can substantially reduce force and acceleration of blunt, direct impacts to mitigate shock energy.

In order to achieve this goal, computational models, via finite element (FE) software COMSOL, are developed to design hyperdamping protective materials having large shock and blast energy absorption capabilities. Promising designs are fabricated and evaluated in the laboratory to verify model predictions and to explore concepts that cannot be as readily modeled. Using the fabricated specimens, experimental studies of impact absorption via force transducer hammer input with force transducer or accelerometer output are undertaken to analyze shock mitigation capabilities.

1.4 Overview of thesis

This thesis is organized as follows. Chapter 2 discusses the initial computation models and model results used to develop specimen designs. Chapter 3 describes the method of specimen fabrication and constraint, as well as the data acquisition system and testing setups used in the experiments for both the force transducer and mini accelerometer output evaluations. Chapter 4 presents the experimental results of the studies and discusses notable trends and their significance towards the use of hyperdamping protective material systems in helmet design. Chapter 5 summarizes the major discoveries of the research and proposes direction for additional research efforts.

2 SINGLE BEAM AND STAGE MODELS

Finite element (FE) software COMSOL Multiphysics is used to create computation models of single beam and stage designs. The computational models study the characteristics of simple designs in order to gain an understanding of key parameters and determine geometric ranges where higher damping is expected to occur. The following sections of this chapter serve to explain the modeling process within COMSOL and discuss the significance of the studies on the design of hyperdamping material systems, as seen in Section 3.1.

2.1 Finite element (FE) modeling

Specifically, pre-stressed eigenfrequency parameters studies are conducted to determine the first eigenfrequency value based on physical parameters of the design. To create the models in COMSOL Multiphysics, material properties, geometry, and constraints must be specified. The following material properties are used to model the linear elastic behavior of the silicone rubber elastomer of the hyperdamping material systems when operating dynamically with infinitesimal strains: Young's modulus of 752,000 Pa, density of 1100 kg/m^3, and Poisson's ratio of 0.49. These parameters model the elastomer material used in the fabrication of the specimens. Young's modulus and density are determined experimentally, while Poisson's ratio is assumed based on common values of other similar rubbers

Figure 3 shows example single beam and stage geometries and constraints. For both the single beam and single stage models, discussed in more detail in Sections 2.2 and 2.3, respectively, two main parameters (1) the ratio of beam width to beam length and (2) the ratio of prescribed displacement to beam length. Similarly, the constraints on both are such that the top of the geometries is constrained with the prescribed displacement in the y-direction and zero displacement in the x, while the bottom has zero displacement in the y but is free in the x. For this study, strain refers to the ratio of prescribed displacement to the total unconstrained height.

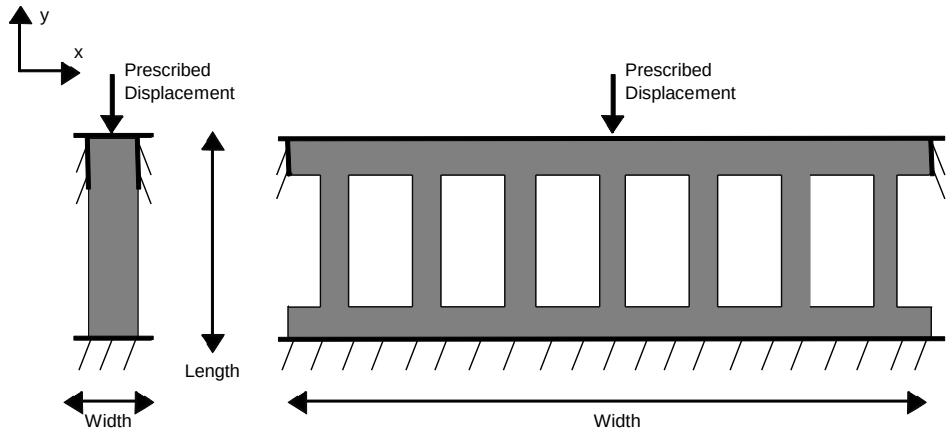

Figure 3: Prescribed displacement and other constraints set on example geometries for single beam (left) and stage (right) models in COMSOL

Geometric parameters are set such that all beam lengths are 0.003175 m, the entire geometric length is 0.00508 m, and void widths are 0.0015875 m. These values are used to accommodate the limitations of the fabrication method discussed in Section 3.1 while maintaining dimensions that are acceptable for use within helmet shock absorbers. The ratio of beam width to beam length, ratio of prescribed displacement to beam length, beam width, and prescribed displacement are used as parameters in the undertaking of the following models. Both ratios are set to arbitrary values (0.1 for beam width ratio and 0.001 for prescribed displacement ratio), to be changed later in the parametric study. The beam width is set to the ratio of beam width to beam length times the beam length. The prescribed displacement is set as the ratio of prescribed displacement to beam length times the beam length.

After the desired geometry is created, the property values from the parameters are used to match the property values of the material used in fabrication. Two Prescribed Displacements are added to match the constraints seen in Figure 3. These Prescribed Displacements are geometric constraints set within COMSOL. In the first Prescribed Displacement, the top of the geometry is given the desired displacement from the parameters (ref. Figure 3) in the negative y-direction and zero displacement in the x-direction. For the second Prescribed Displacement, the bottom of the geometry is given zero displacement in the y-direction. This specific set of constraints are used such that the displacement compresses the geometry in the y-direction to lead to buckling. The x- and y- Prescribed Displacements at the top of the geometry force the geometry to undergo the compression. Having zero displacement in the y-direction at the bottom of the geometry keeps the geometry from shifting downward due to the displacement at the top. Lastly, there is no fixed displacement in the x-direction at the bottom of the geometry to allow for free sliding motion during compression.

A triangular mesh is set such that there are at least two elements across the thinnest part of the geometry. In this case, a maximum element size is determined as half the smallest beam width. The desired number of eigenfrequencies to examine is set to 50. Two parametric sweeps are added to the study. The first looks at change in beam width while the second looks at change in prescribed displacement. The exact variables and values for each study are explained in more detail in Sections 2.2 and 2.3.

2.2 Single beam model and results

The single beam model gives an understanding of the principles behind hyperdamping material systems. The model investigates how the relationship between the ratio of prescribed displacement to beam length (disp/L) and the ratio of beam width to beam length (w/L) affect the fundamental eigenfrequency of the geometry. The results of the study are displayed in Figure 4. In this study, the beam length is set to a value of 3.175 mm while disp/L ratio and w/L ratio vary.

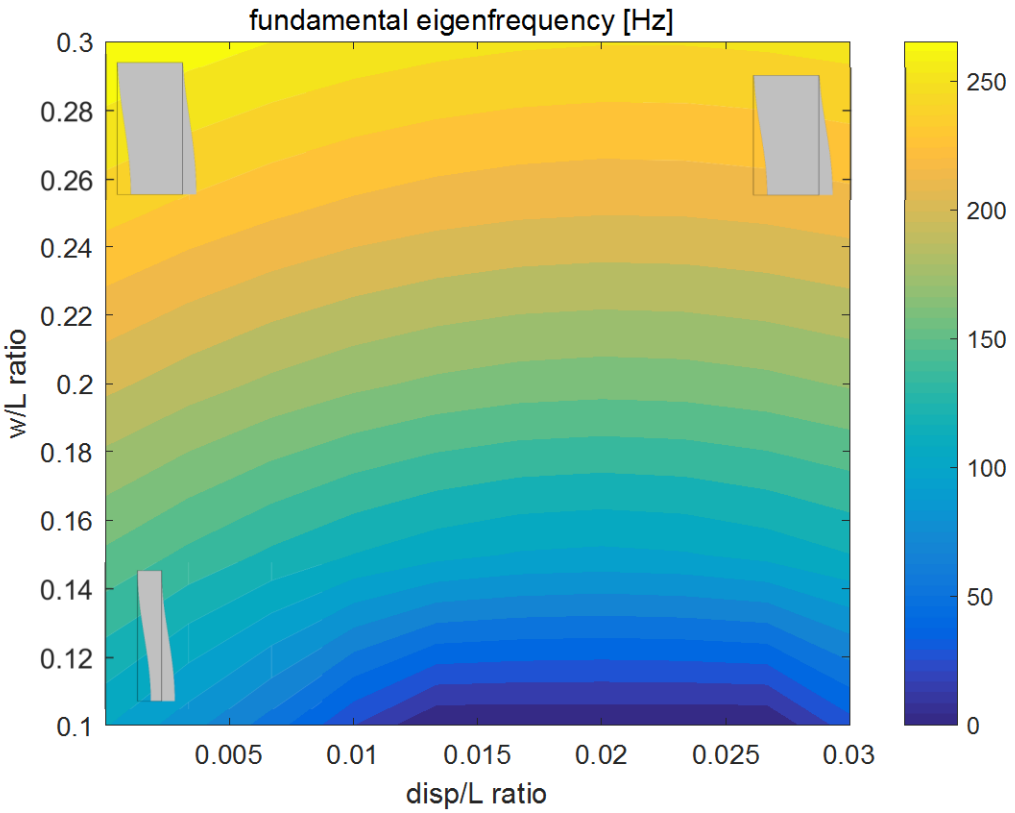

Figure 4: Fundamental eigenfrequency contour plot examining the effects of w/L ratio and disp/L ratio on eigenfrequency for the single beam computational model

In Figure 4 the darkest blue area signifies the location of the lowest fundamental eigenfrequency value. As stated in Equation 1 in Section 1.2, the fundamental eigenfrequency is inversely proportional to damping. Therefore, this region is also likely the area of highest energy absorption. In this case, the ideal beam characteristics are a disp/L ratio around the range 0.01 to 0.027 with corresponding w/L ratio around 0.1. Although smaller values of w/L ratio than 0.1 may also show zero fundamental eigenfrequency, fabrication of these sizes would be difficult and therefore these values are not considered. Overall, fundamental eigenfrequency is lowest with smaller width to length ratio and a displacement to length ratio between 0.01 and 0.027. As such, slender beams are more likely to have a lower fundamental eigenfrequency and consequently are likely to buckle with greater ease. A displacement to length ratio, or strain, of approximately 0.02 leads to near buckling with the most slender beam.

2.3 Linear array model and results

A single stage model geometry is studied computationally in this research. A stage is considered as a single layer array of beams.While a single stage is used in the computational model for simplicity, actual fabricated specimens consist of two stages. This is to provide a middle layer that is free to move in the x-direction, as seen in the sliding of the middle layer in Figure 9 as strain on the specimen increases. In order to compress the specimens in the assembly seen in Figure 10, both the top and bottom of the specimen are fully

constrained in both the x- and y-direction. Considering the desired set of constraints from Figure 3, a second stage is added to allow for the free motion in the x-direction at the bottom in fabricated specimens.

The model geometry considered for this study is a linear, axially symmetric design of increasing beam width from the center. An example geometry is shown in Figure 5. The goal of this computational study is to determine the effect of multiple beam widths on eigenfrequency. The hypothesis is that by having a range of beam width dimensions in a single specimen, the region of critical geometric parameters where the eigenfrequency is zero may broaden. This means that there would be a larger range of displacement-to-length ratio values for which the natural frequency is reduced to vanishing values, and therefore a larger range of displacement-to-length ratio values for which significant damping may occur. Thus, the geometry may be more robust, or have the ability to attenuate impact in a wider variety of impact scenarios and input forces.

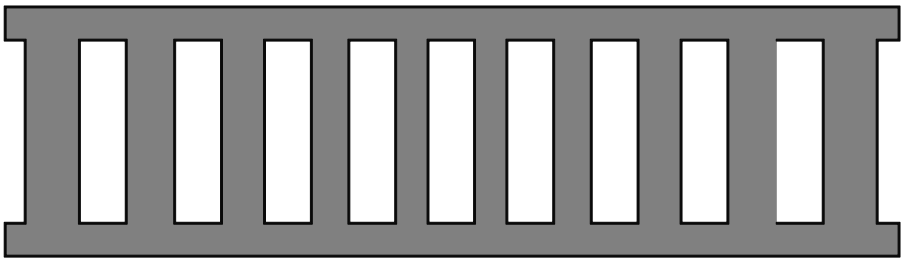

Figure 5: Example linear geometry: axially symmetric design of increasing beam width from center

For the linear geometry, the thinnest beam is in the center with beam width increasing by a set amount for each adjacent beam. This increase in beam width is determined by the parameter Δw, the change in beam width. Δw is a value of beam length. A Δw of 0.02 increases the beam width by 2% of the beam length for each beam adjacent to the center beam. Since beam length does not change, Δw remains the constant for the geometry and the beam width increases linearly with beam number.

The effect of changing beam width and prescribed displacement on the fundamental eigenfrequency of a single stage of the hyperdamping [noun needed] is shown in Figure 6. In this study, beam length remains set at 3.175 mm while disp/L ratio and Δw vary.

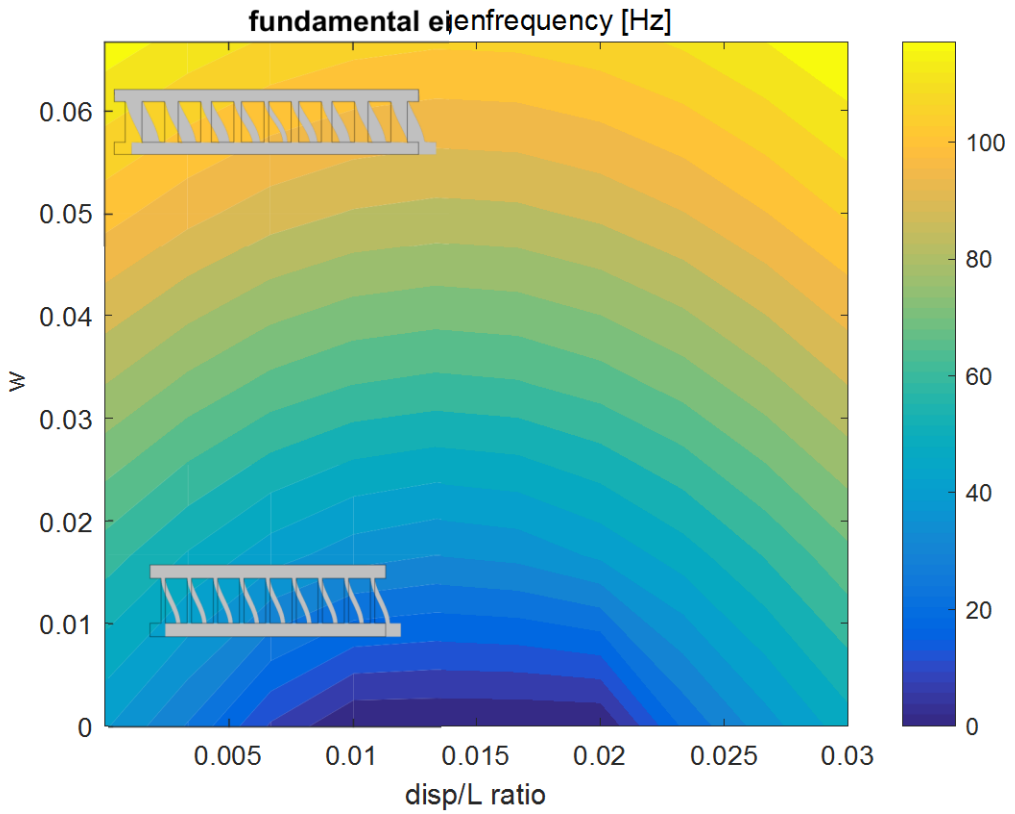

Figure 6: Fundamental eigenfrequency contour plot examining the effects of linear change in beam width and disp/L ratio on eigenfrequency for the linear geometry computational model

Figure 6 shows that a Δw of 0 and a d/L ratio between 0.01 and 0.02 provide the geometry with the lowest fundamental eigenfrequency as this is the region with the darkest blue color. This complements the results of the single beam study, showing that thin beams have a lower fundamental eigenfrequency at a given prescribed displacement. Since having a lower fundamental eigenfrequency is indicative of increased damping, the dark blue region is where highest energy absorption is likely to occur for this geometry. Therefore, based on the results of this model, it may be preferable to have a larger number of equally thin beams (Δw of 0) than a variety of beam sizes when desiring low fundamental eigenfrequency. The results seen here look only at the fundamental eigenfrequency where global buckling occurs at the Δw of zero. Additional local modes can be seen at higher eigenfrequencies. The third eigenfrequency, especially, shows a local buckling mode at Δw of 0.06.

In this case, a disp/L ratio near 0.015 provides the necessary constraint to be near buckling. This is lower than the constraint needed for the single beam design due to the increased length of the linear array from the top and bottom layers. Though the actual beam lengths are the same in both designs, the displacement to length ratio uses total length of the design. Therefore, the linear array design has a larger total length than the single beam. Both designs buckle near the same value of prescribed displacement when accounting for the larger length of the linear array.

3 EXPERIMENTAL METHODS

Specimens must be designed and fabricated for testing in order to assess the shock mitigation of hyperdamping protective material systems. **Error! Reference source not found.**, discusses the selected designs of the specimens for fabrication and testing. Eight specimens and a control are fabricated for testing. One specimen consists of a uniform array of beams. Four specimens consist of non-uniform beam widths, two with increasing beam widths from the center and two with decreasing beam widths from the center. Three specimens consist of beams with randomly assigned beam widths. The control is a solid mass of elastomer used for comparison purposes and to show specimen trends as properties of geometry and not material.

The following section, 3.1, explains specimen design and the method involved with fabricating the specimens. The general procedure of fabrication involves pouring pre-cured silicone rubber into 3-D printed molds. This specific fabrication method is used to allow for the production of varied geometries with the desired material properties of the silicone elastomer.

Sections 3.2-3.6 describe the experimental setups related to testing of the specimens. The three experimental setups are (1) load frame assessment, (2) force transducer evaluation, and (3) accelerometer evaluation. The load frame assessment is used to determine the static properties of each of the specimens. The force transducer and accelerometer evaluations are used to examine the force and acceleration reduction capabilities of the specimens.

3.1 Specimen design and fabrication

From the results of the computational studies in Sections 2.2 and 2.3, it is hypothesized that having a thinner beam arrangement results in better shock mitigation. To test this hypothesis, one specimen, the Uniform, is designed with uniform beam widths. Two additional specimens, lv2-wp79375-dw02 and lv2-wp79375-dw06, adhere to the linear array arrangement discussed in Section 2.3 with increasing beam width from the center. Five more specimens are designed to assess whether or not the location of thin and thick beams along the cross-section of a specimen geometry plays a role in shock mitigation. Two designs, rv2-wp79375-dw02 and rv2-wp79375-dw06, follow a linear arrangement similar to that of Section 2.3 but have decreasing beam width from the center. An additional three designs, the rand-var, have randomly assigned widths for all beams. Lastly, a bulk mass design is used as a control to compare against the other specimens and show specific results are a consequence of hyperdamping protective material design and not the host material.

Error! Reference source not found. describes the specimens created for testing. The Uniform is created with uniform beam widths of 0.79375 mm. Two values for change in beam width, Δw, are chosen: 0.02, and 0.06. These designs have a increasing beam width from the center. Similarly, a "reversed linear" design is selected for fabrication with a design of decreasing beam width from the center with the same Δw as the linear designs. Here the smallest beam width remains 0.79375 mm at the two edge beams of the design. Lastly, the three random designs are created with randomly assigned beam widths between values of

0.79375 mm and 1.74 mm. This range of beam values is based on the beam width range of the lv2-wp79375-dw06 specimen, which has the widest range of beam width values of the specimens. A control, as a solid mass of elastomer, with the same major dimensions as the rand-var-02 specimen is also molded for testing.

The smallest beam width is set to 0.79375 mm, a w/L ratio 0.25, due to the limitations of the specimen fabrication discussed in Section 3.1. All eight specimens are made with eleven beams and two stages. While a single stage is used in the computational model for simplicity, actual fabricated specimens consist of two stages. This is to provide a middle layer that is free to move in the x-direction, as seen in the sliding of the middle layer in Figure 9 as strain on the specimen increases. In order to compress the specimens in the assembly seen in Figure 10, both the top and bottom of the specimen are fully constrained in both the x- and y-direction. Considering the desired set of constraints from Figure 3, a second stage is added to allow for the free motion in the x-direction at the bottom.

Table 1: Specimen design and description

Specimen	Description
Uniform	Axially symmetric design with beam widths of 0.79375 mm
lv2-wp79375-dw02	Axially symmetric design of increasing beam width from 0.79375 mm at the center, increasing at 2% of the beam length (0.0635 mm)
lv2-wp79375-dw06	Axially symmetric design of increasing beam width from 0.79375 mm at the center, increasing at 6% of the beam length (0.1905 mm)
rv2-wp79375-dw02	Axially symmetric design of decreasing beam width from 0.79375 mm at the edges, decreasing at 2% of the beam length (0.0635 mm) from the center
rv2-wp79375-dw06	Axially symmetric design of decreasing beam width from 0.79375 mm at the edges, decreasing at 6% of the beam length (0.01905 mm) from the center
rand-var-01	Asymmetric design with random beam widths
rand-var-02	Asymmetric design with random beam widths
rand-var-03	Asymmetric design with random beam widths
Control	Solid mass of elastomer with same major dimensions as rand-var-02

The files of the mold geometry are first made in SOLIDWORKS as seen in Figure 7**.** Each mold consists of a base and a shell, seen on the right and left, respectively, in both the top and isometric views of Figure 7. A FlashForge 3d Printer Creator Pro is used to print the molds from the part files. A value of 0.175 mm is used to augment the dimensions in SOLIDWORKS in order to account for the filament compaction during printing.

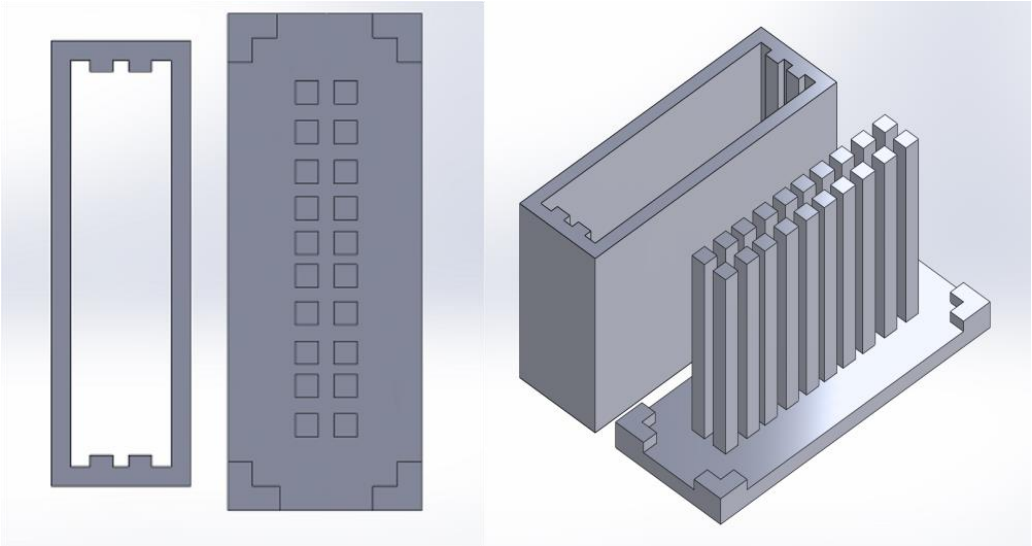

Figure 7: SOLIDWORKS mold with shell (left) and base (right) in both top and isometric views for rand-var-03

After the molds are printed, the shells are set on the base using wax. The specimens are fabricated by pouring pre-cured silicone rubber into the molds and setting overnight. The specimens are demolded the next day, washed with cold water to remove loose strings of silicone and wax from the mold, and allowed to dry. Table 2 shows the mass and unconstrained length of the specimens. Figure 8 shows nine total specimens after fabrication. Here, the unconstrained length is the total length of the specimens with both stages. The desired unconstrained length of the specimens is 12.5 mm. While the specimens are all below this value, they have a standard deviation of 0.1634 mm and are within 1.5% of the mean unconstrained length.

Table 2: Fabricated specimen properties mass and unconstrained length

Specimen	Mass [g]	Unconstrained Length [mm]
Uniform	10.026	12.2047
lv2-wp79375-dw02	10.644	12.4206
lv2-wp79375-dw06	12.280	12.2047
rv2-wp79375-dw02	10.769	12.0015
rv2-wp79375-dw06	11.663	12.0777
rand-var-01	11.801	11.8364
rand-var-02	12.445	12.0650
rand-var-03	12.551	12.0142
Control	16.479	12.0650

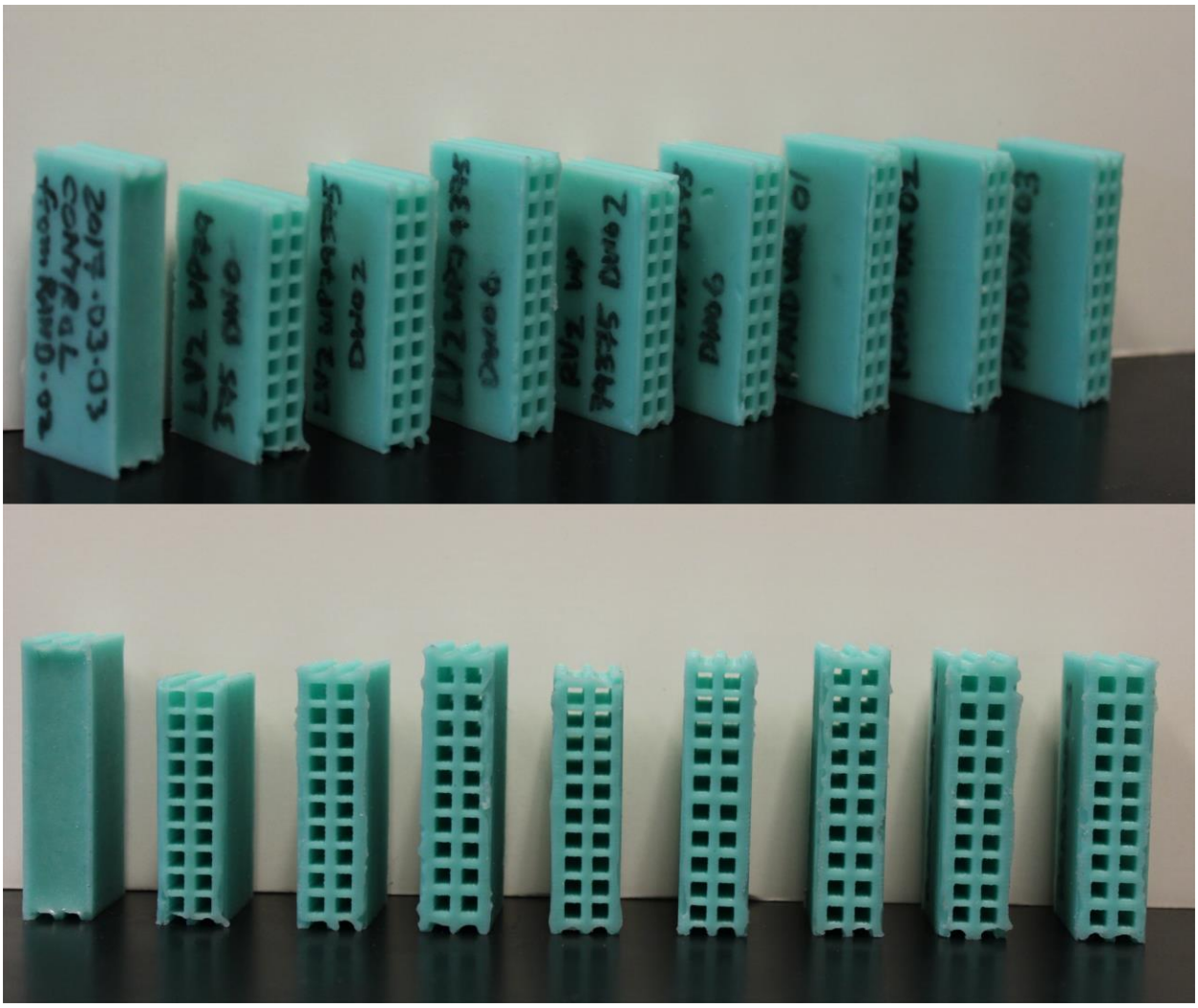

Figure 8**: Fabricated specimen photos. Here the specimens are presented in the following order, from left to right: control, Uniform, lv2-wp79375-dw02, lv2-wp79375-dw06, rv2-wp79375-dw02, rv2-wp79375-dw06, rand-var-01, rand-var-02, and rand-var-03**

3.2 Experiment overview

There are three experimental setups utilized in this research: (1) load frame assessment, (2) force transducer evaluation and (3) mini accelerometer evaluation. Specimen designs for the eight specimens and control are discussed in Section 3.1. All nine specimens can be seen in Figure 8. All nine specimens are assessed via load frame for material properties. For the force transducer and accelerometer setups, each specimen except the control is compressed at five different lengths from unbuckled to very noticeably buckled. These varying lengths of compression are known as levels of constraint or strain. Since each specimen has a different geometry, the specimens buckle at different values of strain. Also considering the mechanism used for specimen constraint, discussed in Section 3.4, it is difficult to compress the geometries to specific values of strain. Therefore, the five levels of constraint are generally as follows: (1) 0.5%-6% strain, (2) 6%-14% strain, (3) 14%-20% strain, (4) 20%-25% strain, and (5) > 25% strain. Figure 9 shows the lv2-wp79375-

dw02 specimen at completely unconstrained and five different levels of constraint, where buckling occurs between the 2nd and 3rd levels of constraint (not including the unconstrained level). It is difficult to compress the control since it consists of a solid mass of elastomer. Therefore, only a single level of constraint is used in both experimental setups for the control. For all of three experimental procedures, the MATLAB data acquisition toolbox is used to read analog input signal from all sensors and filter and process the data.

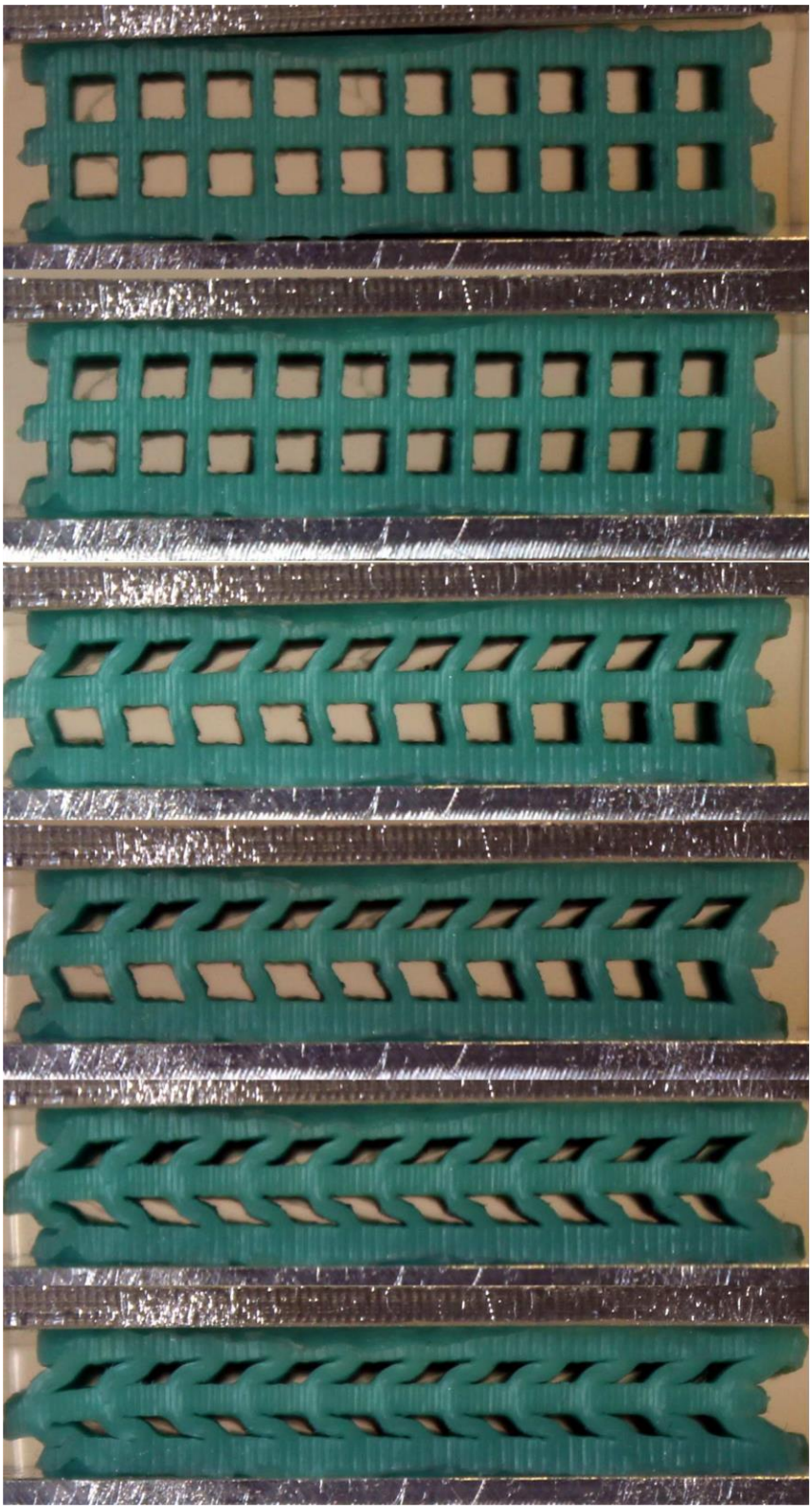

Figure 9: Specimen lv2-wp79375-dw02 shown at different levels of constraint during testing

From the top down, the levels of constraint are: unconstrained, 5.52%, 10.94%, 17.18%, 24.13%, and 28.83% strain.

3.3 Load frame assessment

The load frame assessment is used to determine static properties of the specimens. A load cell (PCB 110205A) and signal conditioner (PCB 8162011A) are used to measure one-dimensional force on the specimen while a laser displacement sensor (Micro Epsilon ILD1700) is used to measure the displacement of the specimen.

For this assessment, each specimen is displaced approximately 5.25 mm in length. Due to the difficulty in compressing the control, the control is displaced by approximately 1.75 mm. Before each test, the specimen is "exercised" by displacing the specimen twice to settle the direction of buckling. Once the data acquisition has begun, the specimen is displaced at a rate of 2.1 mm/min. This rate is chosen as the fastest displacement possible while still obtaining the appropriate trends for the load cell and laser displacement sensor setup.

The MATLAB data acquisition toolbox is used to read in the signals from the sensors. An example MATLAB code can be found in the Appendix. The data is sampled at a frequency of 256 Hz and is filtered with a low-pass filter at 35 Hz. The data is then used to look at force and stiffness as a result of strain.

3.4 Specimen setup and constraint

The force transducer and accelerometer evaluations involve assessing the specimens at different levels of strain. Two aluminum 6063 plates with 1/8" thickness are used to provide the constraint for the specimens. The aluminum plates are used to give a uniform constraint on the specimen while also providing an even surface for impact. In order to compress the specimen, a guitar tuner in combination with fishing line is used to change the distance between the two plates. One aluminum plate is machined larger to accommodate the guitar tuner. The guitar tuner (YMC Chrome Tuning Peg Round 220-3L3R) is mounted on end of the larger plate. The specimen is placed on top of the plate and is sandwiched between the two plates. Fishing line (Tebco Omniflex 50 lb 0.029 dia) is used to constrain the specimen between the plates using four holes on each plate surrounding the specimen. For each corner, fishing line is knotted on the end of the small plate, pulled through the corresponding hole in the large plate, and fed through the guitar tuner. The plates are adjusted as uniformly as possible before tightening the guitar tuner. The specimen assembly can be seen in Figure 10. The constraint on the specimen can be adjusted by turning the guitar tuner.

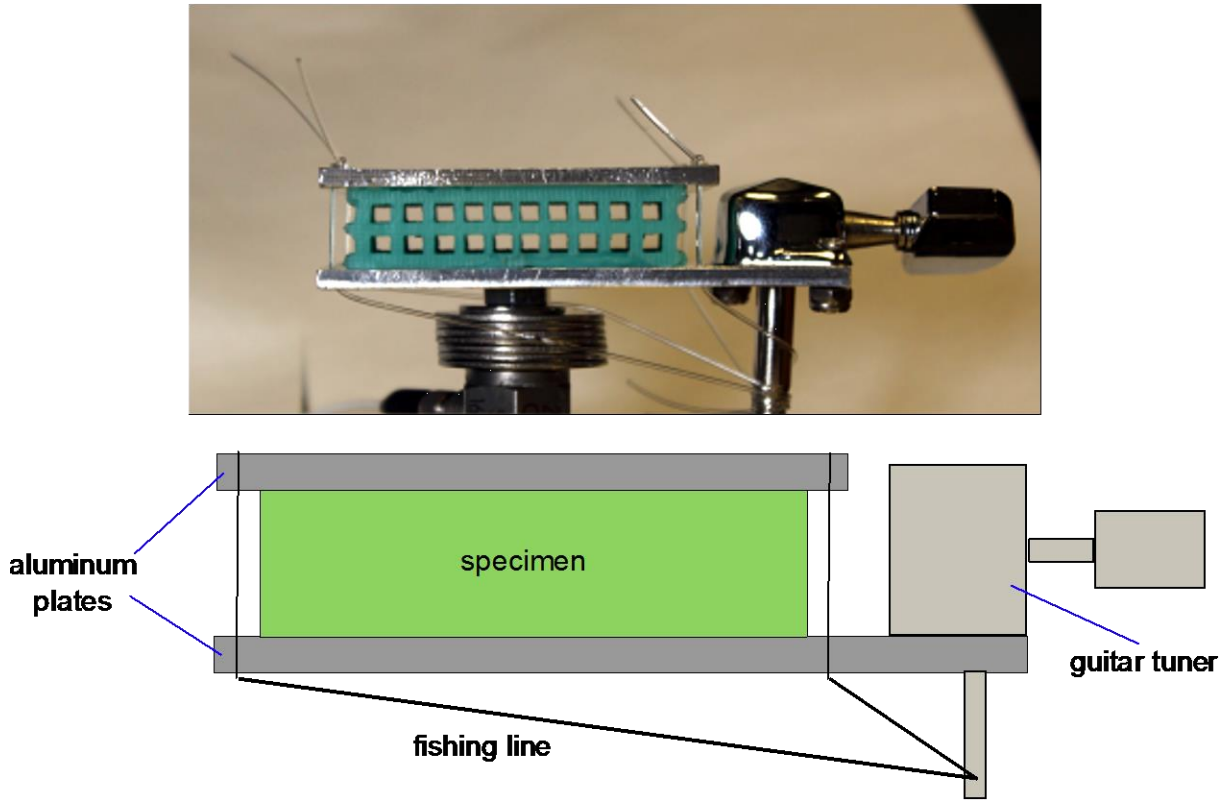

Figure 10: Aluminum plate and guitar tuner assembly is used to provide constraint to the specimen. Top shows specimen assembly in experimental setup while bottom depicts simplified model of assembly

3.5 Experimental setup 1 – impact hammer and force transducer

The first experimental setup assesses the force reduction through the specimen upon impact from one side. A modal hammer (PCB 086C01) with a reactionary mass is used to impart a known force amplitude on the specimen assembly while a force transducer (PCB 208C02) is used to measure the time series output force that is transmitted through the specimen. For this setup, a 10-32 screw is screwed onto the large plate of the specimen assembly where the center of the specimen would reside. In order to account for the length of the guitar tuner end, a nut and washers are added onto the end of the screw. The force transducer is mounted onto the SMART TABLE UT2 isolation table, on which the experiments are conducted. The specimen assembly is then screwed into the force transducer. This setup can be seen in Figure 11.

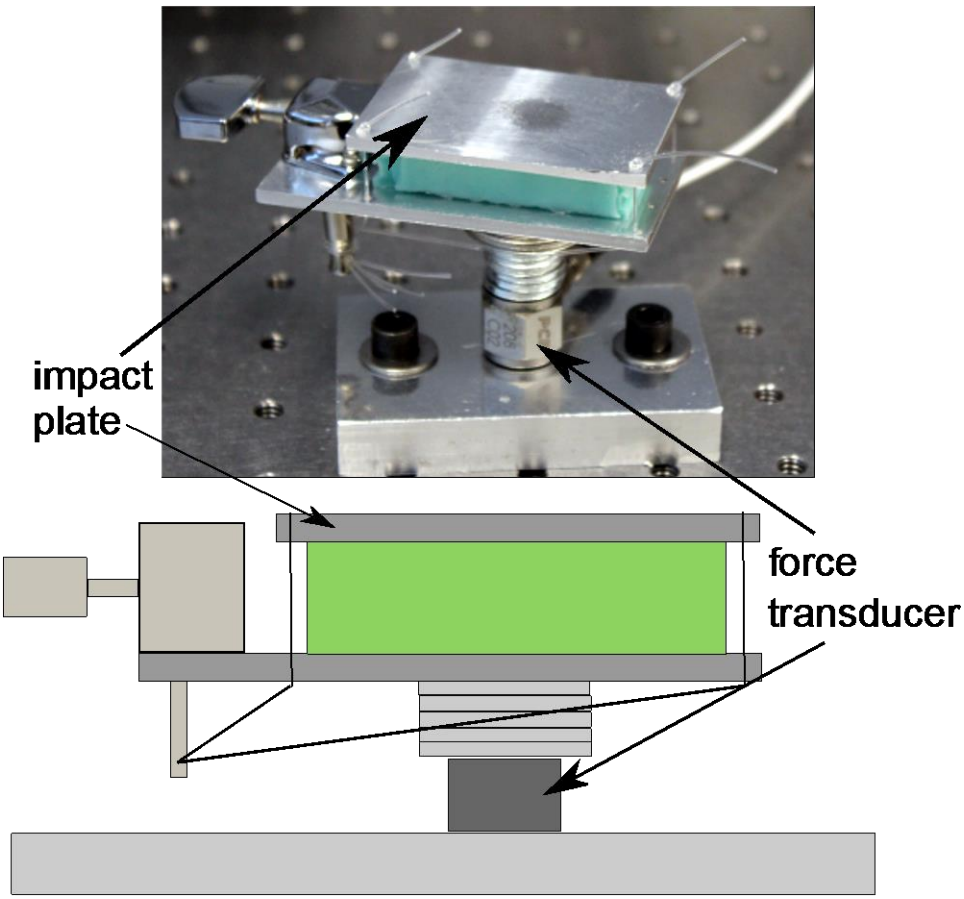

Figure 11: Experimental setup 1 shown for the control (top) and simplified model (bottom) where the specimen assembly is mounted on the force transducer and bolted to the isolation table

The procedure for each test is as follows. The specimen constraint is adjusted via the guitar tuner to approximate desired value. Each corner of the specimen is measured using digital dial calipers (iGaging OrignCal) to assure uniform constraint. If the level of constraint is not uniform, the large plate is held down while the small plate is adjusted by pulling or pushing on the corner where the dial caliper measurement is different from the desired measurement value. The level of constraint is considered uniform if all four corners read within 0.0254 mm of each other. Once the level of constraint has been adjusted, the data acquisition can begin. The modal hammer is used to hit flat against the center of the small plate with varying force (~ 50 N to 450 N) for 100 hits. This force ranges adequately covers the working range of the modal hammer, thus ensuring high quality force input data is obtained. The output forces are likewise found to fall within the ideal working range of the force transducer used below the specimen. Continuous use of fishing line past two uses makes it difficult to adjust the plates for uniform constraint and causes the fishing line to snap easily under tension. This is due to the edges of the holes in the aluminum plates cutting into the fishing line and making notches. Adjusting the fishing line from the guitar tuner then becomes increasingly difficult as the notches on the line get caught on the edges of the holes in the aluminum. Therefore, the fishing line for the assembly is generally replaced after every 2 specimens from the wear and tear.

The MATLAB data acquisition toolbox is used to read analog input signal from both sensors. The sampling frequency is 131072 Hz. This is much higher than the sampling frequency of the load frame assessment to avoid aliasing. The data needs to be able to accurately record peaks in the signal in order to compute decay rate in the post-processing. The signal conditioner output wires into an NI SCB-68A which is wired into an NI PXIe-6368 card. The card is inserted into the NI PXIe-1073 chassis and the system is connected to a Windows 7 PC. The script is written to ensure that a minimum of 40 N input force from the modal hammer is required for the data to be recognized as a "hit" and saved. Data is captured for 2 seconds after each hit, for 100 hits per specimen constraint level, with five levels of constraint for each specimen except the control. The level of constraint varies from 0.5% to 27% strain. Once the data is acquired, all channels are digitally filtered with a low-pass filter at 50 Hz and a high-pass filter at 18000 Hz. The FFT of the data is taken over 1 second after each hit. The decay rate of the impulse response and octave band measures of the force output to force input for 125 Hz to 16,000 Hz are then computed.

3.6 Experimental setup 2 – impact hammer and mini accelerometer

The second experimental setup studies the acceleration upon impact. Once again, a modal hammer (PCB 086C01) is used to impart a known force amplitude on the specimen assembly. In this setup, the specimen assembly is free to move upon impact. A mini accelerometer (PCB U352A10) is attached to the center back of the specimen assembly using wax. Fishing line is used to hang the assembly in a frame mounted on the SMART TABLE UT2 isolation table. This setup can be seen in Figure 12.

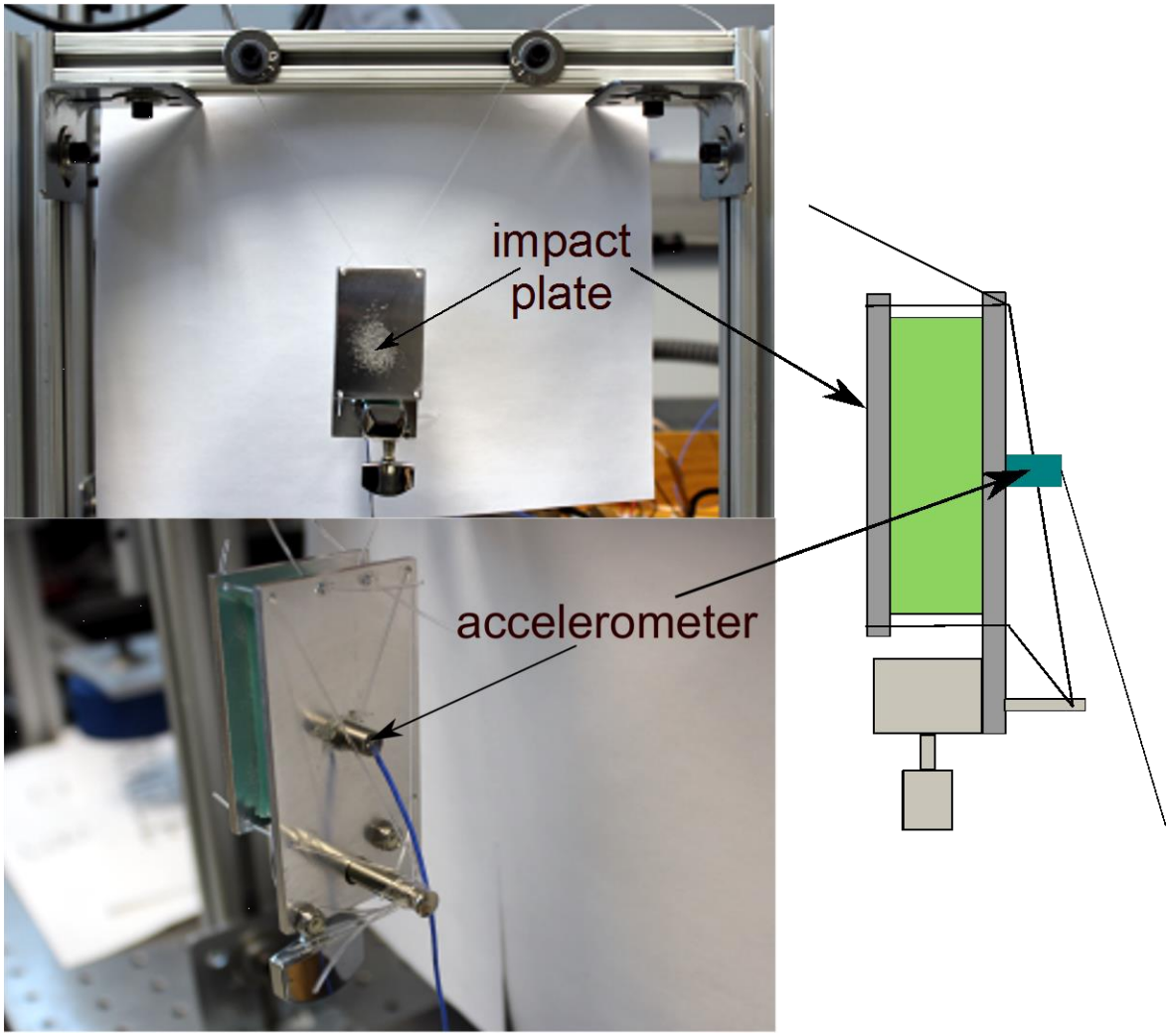

Figure 12: Experimental setup 2 shown for the control (left) with a simplified model (right). Top left shows the front of the setup and the hanging arrangement while bottom left shows the back where the accelerometer is mounted

The procedure for each test is similar to that of the first experimental setup. The specimen assembly is hung on the frame with the small plate facing away from the isolation table and tightened in place. The specimen constraint is adjusted via the guitar tuner to near the desired constraint level. The digital dial calipers are used to measure the constraint at each corner of assembly. The constraint is considered uniform if all corners are within 0.0254 mm of each other. The mini accelerometer head is coated in wax and attached to the back of the assembly at the center of the specimen position. The data is once again taken for 100 hits with the modal hammer with varied force (~ 50 N to 400 N in this setup), hitting flat against the small plate. After each hit, the specimen is given some time (~ 1 second) to swing freely. The specimen should be relatively motionless before each hit and should come to a forced stop between hits after being allowed free movement. Similarly to the force transducer evaluation setup from Section 3.5, the fishing line connecting the two aluminum plates experiences considerable wear and tear. During testing, the line is caught on the edges of the holes on the plates. This worsens from the force transducer evaluation setup due to the violent swinging movement that occurs upon impact. Often the line stretches thin during plate adjustment after

being stuck on the edge of the hole. Thus, fishing line for the assembly is replaced with every change in specimen. After every test, the fishing line used for hanging is retightened and the accelerometer is once again firmly pressed against the assembly to ensure it will stay in place.

The MATLAB data acquisition and post-processing uses the same script as the first experimental setup with adjustments in output sensor sensitivity and units. An example MATLAB code used for the data acquisition and post-processing can be seen in the Appendix. The FFT is taken over 0.10 seconds instead of 1 second after each hit to adjust for the movement involved with the new setup.

4 RESULTS AND DISCUSSIONS

The goal of this research is to assess the capacity of hyperdamping protective materials systems for shock mitigation. In that regard, eight specimens are fabricated to exhibit hyperdamping properties while a control of solid mass is used for comparison in testing. All nine specimens are tested in three experimental setups discussed in Sections 3.3, 3.5, and 3.6. The following chapter displays and discusses the results of the three experiments. The first experiment determines the material properties of specimens in a load frame analysis. The second examines direct force reduction of each specimen at five levels of constraint in a force transducer evaluation. The third examines reduction in acceleration as compared to the control for the specimens at different levels of constraint in an accelerometer evaluation. The force and accelerometer evaluations are especially important in characterizing the success of hyperdamping material systems to provide considerable shock mitigation using less mass than the control specimen.

4.1 Static load frame results

Two key relationships are discussed from the results of the load frame assessment: the relationship between force and strain and the relationship between stiffness and strain for each specimen. The results of the load frame assessment can be seen in Figure 13 and Figure 14.

Figure 13 displays the relationship between load and strain for all of the specimens. Figure 13a compares the Uniform (red), lv2-wp79375-dw02 (green), and lv2-wp79375-dw06 (blue) specimens. Figure 13b compares the Uniform (red), rv2-wp79375-dw02 (green), and rv2-wp79375-dw06 (blue) specimens. The Uniform (red), rand-var-01 (green), rand-var-02 (blue), and rand-var-03 (cyan) specimens are compared in Figure 13c. Lastly, the Uniform (red) and control (green) are compared in Figure 13d.

The curves of load to prescribed displacement for the specimens generally consist of three regions: (1) initial incline, (2) flat portion, and (3) final linear incline. The initial incline seen in the low strain region of the plots shows the increasing load for small values of strain. The flat portion of the curve depicts where buckling may occur for the specimen if it occurs at all. Specifically, buckling occurs in the specimen if force decreases with stiffness. Lastly, the final linear incline shows the increase in load and strain seen during compaction, when the specimen is fully compressed. The hysteresis observed in the force curves are a result of the finite rate of displacement on the specimen during testing.

In Figure 13a, increasing beam width causes buckling to occur at a larger value of strain while compaction occurs at a lower value of strain. Maximum load also increases with increasing beam width. The results of the load frame assessment for the lv2-wp79375-dw06 (blue) match with the results of the rand-var specimens in Figure 13c. The rand-var specimens overlap in their results and show the same trend. It is hypothesized that since the rand-var specimens have comparable beam width variation to that of the lv2-wp79375-dw06, they may exhibit similarmechanical properties. This suggests that there is not much influence in utilizing a linear change in beam width across a stage, but rather it is the overall range of beam width values that more strongly influences the mechanical properties of the specimens.

Yet, in Figure 13b, it can be seen that the rv2 specimens (green and blue) do not show a decrease in force with strain in the middle portion of the curve where buckling should occur. This suggests that the rv2 specimens do not buckle during the testing. Rather, because the slopes are reduced in FIGURE 13B in the middle region of the load-displacement curves, this suggests that the rv2 specimens soften considerably while not specifically undergoing a buckling phenomenon. From this, it can be reasoned that an organized cross-section of the specimen with the widest beam in the center of the geometry and smaller beam widths at subsequent, adjacent neighbors inhibits conventional buckling, because all the other specimens, including the rand-var, are able to buckle.

The control (green) in Figure 13d does not display the same trends as the other specimens. As a solid mass of elastomer, it is unable to buckle and instead has a mostly linear relationship between force and strain. The control also cannot be compressed to the same values as the other specimens due to being a solid mass.

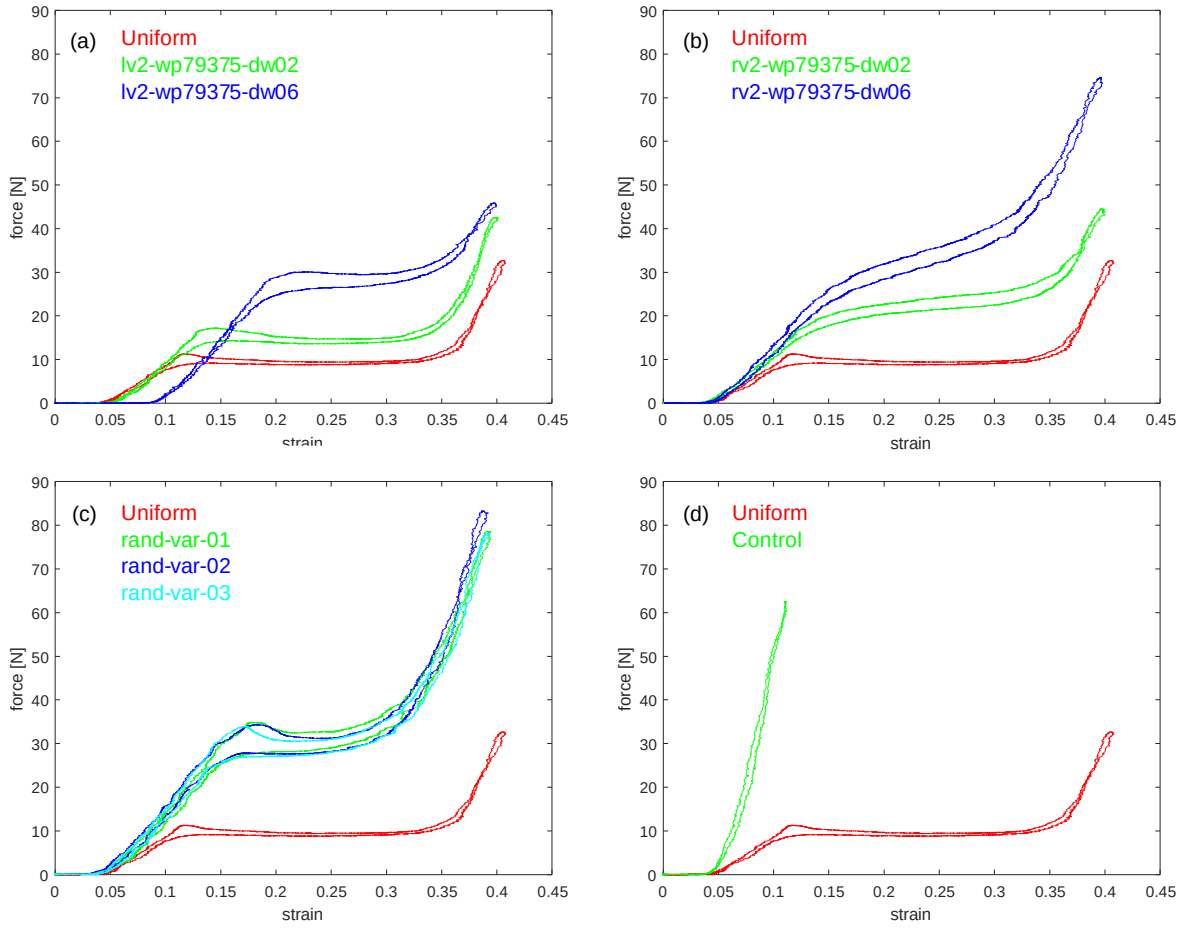

Figure 13: Load frame assessment results displaying the relationship between force and strain for each specimen. (a) Uniform (red), lv2-wp79375-dw02 (green), and lv2-wp79375-dw06 (blue); (b) Uniform (red), rv2-wp79375-dw02 (green), and rv2-wp79375-dw06 (green); (c) Uniform (red), rand-var-01 (green), rand-var-02 (blue), and rand-var-03 (cyan); (d) Uniform (red) and control (green)

Stiffness as a function of strain for each specimen is presented in Figure 14. Figure 14a compares the results of the Uniform (red), lv2-wp79375-dw02 (green), and lv2-wp79375-dw06 (blue) specimens. Figure 14b compares the results of the stiffness for the Uniform (red), rv2-wp79375-dw02 (green), and rv2-wp79375-dw06 (blue) specimens. In Figure 14c, the Uniform (red) is compared to the rand-var-01 (green), rand-var-02 (blue), and rand-var-03 (cyan) specimens. Lastly, Figure 14d compares the stiffness-strain results for the Uniform (red) and control (green) specimens.

A zero or negative value for stiffness is due to buckling. This is the region where the fundamental eigenfrequency vanishes and damping is highest for the specimen. The Uniform specimen (red) has buckling occur for the longest range of strain values for all the specimens. As seen in Figure 14a, this region shifts to the right and occurs for a shorter range of strain values with increasing beam thickness. In Figure 14c, the rand-var specimen results align exactly, showing the same strain values for zero or negative stiffness. Although the lv2-wp79375-dw06 specimen requires a slightly higher strain (0.25) than the rand-var (0.20), the curves have the same shape.

From Figure 14b, it can once again be seen that the rv2 specimens do not exhibit buckling, as they do not drop all the way to zero stiffness. The control in Figure 14d also does not show zero stiffness since the solid mass of elastomer cannot buckle and can only be compressed to about a fourth of the strain range of the other specimens.

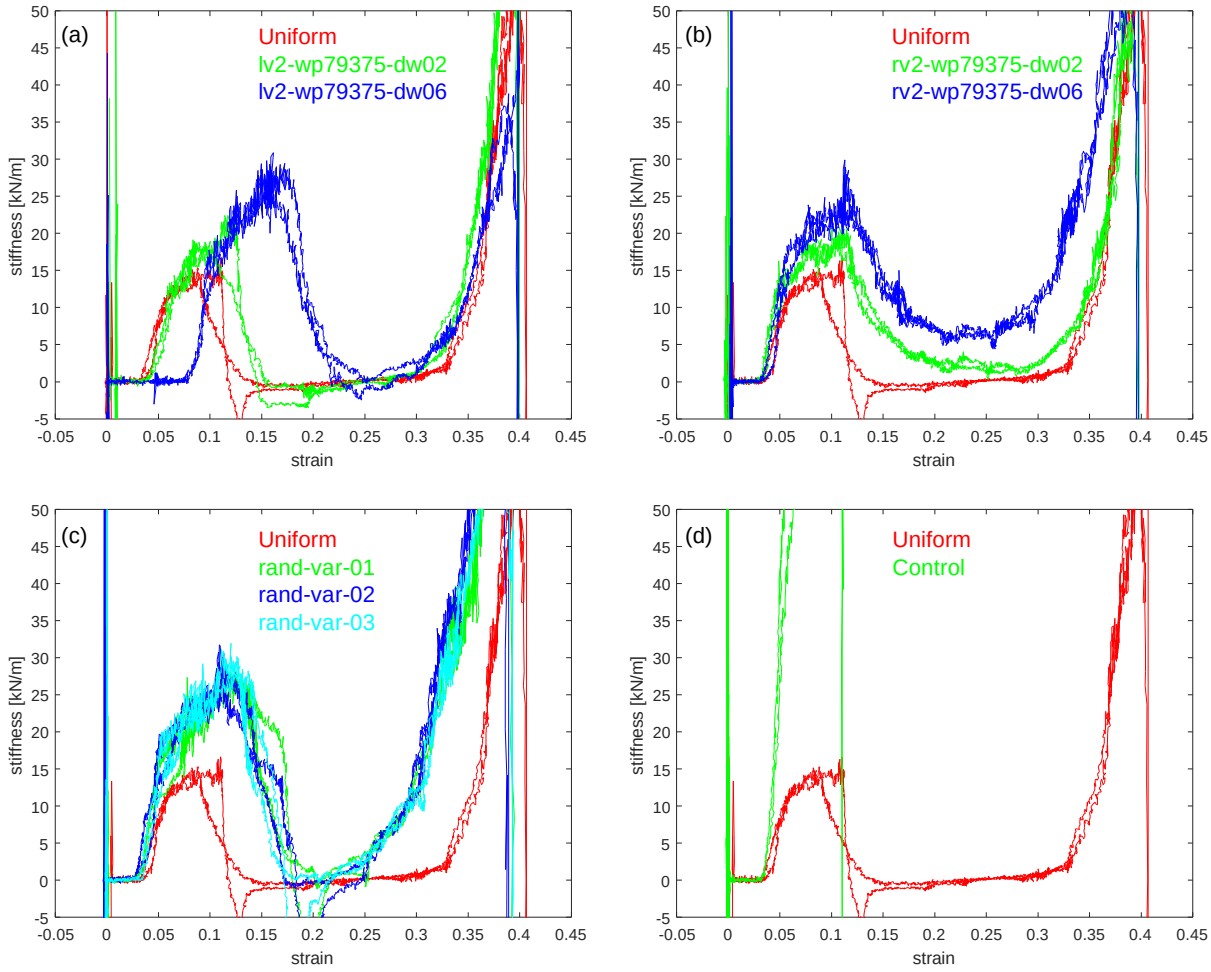

Figure 14: Load frame assessment results displaying the relationship between stiffness and strain for each specimen. (a) Uniform (red), lv2-wp79375-dw02 (green), and lv2-wp79375-dw06 (blue); (b) Uniform (red), rv2-wp79375-dw02 (green), and rv2-wp79375-dw06 (green); (c) Uniform (red), rand-var-01 (green), rand-var-02 (blue), and rand-var-03 (cyan); (d) Uniform (red) and control (green)

4.2 Impact hammer and force transducer results

The impact hammer and force transducer evaluations of the specimen assess key factors relating to force reduction and validation for the use of hyperdamping material systems in helmets and protective head gear. The decay rate of the impulse response and peak force output are determined for each test.

The decay rate is the rate at which the oscillatory time response of output force exponentially decays to zero. A larger (absolute) value of decay rate is indicative of more rapid attenuation of the input force and, oftentimes, of greater damping capacity for the material system. A faster decay is ideal for shock mitigation in protective headgear since it results in faster dissipation of transmitted force that may ultimately be received by the skull. In general, specimens with larger values of decay rate exhibit greater potential for shock damping.

The comparison of output force to input force displays the force reduction capability of each specimen. A steeper slope in the relationship between output force to input force indicates worse force reduction. Specimens with lower values of output force are therefore better for protective material system applications.

In Figure 15, the decay rate and output force are displayed as a function of input force for the control specimen. These values are used as a comparison for decay rate and output force for the eight specimens later in this section. For the control, the decay rate is independent of the input force amplitude, consistently near a value of -200.

The control specimen possesses a linear relationship between input and output force, as seen from the constant slope in Figure 15. This slope has an approximate value of 0.36 N/N, meaning that the solid mass of elastomer transmits approximately 36% of the input forces between around 75 to 300 N.

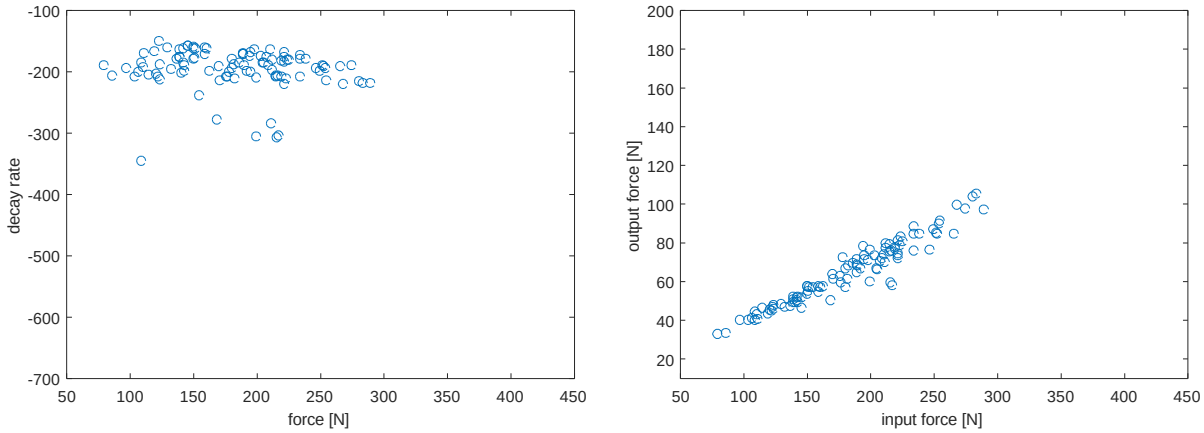

Figure 15: Decay rate (left) and output force (right) as a function of input force for the control specimen in the force transducer output experiment

Figure 16 displays the decay rate for each specimen against the amplitude of the input impact force for the eight specimens. Each plot contains the five levels of constraint from blue, red, magenta, green, and black for increasing level of strain and brown diamonds representing the control values from Figure 15.

The decay rate varies between values of -500 and -30. Higher levels of constraint correlate with increased damping. This is discussed more thoroughly later in this section. The overall trend of the data is an arch or upside down U. There is more spread, or a wider range of decay rate values for a given input, force at low (<150 N) and high (>300 N) forces. The decay rate in these regions is also of greater value than for the mid-range force input, which can specifically be seen in Figure 16g. This suggests that there is less damping with input forces within 150 N and 300 N and that the specimens may be more proficient at attenuating impacts outside of this region, although the decay rate values within this region are not considerably lower than those outside of the region. The top of the curves are also flatter than the bottom portion, suggesting that each specimen has a minimum decay rate value across the mid-range of force inputs (~ 150 to 300 N).

There are differences to be seen in decay rate between the specimens at corresponding levels of constraint. For the least constraint (blue), the Uniform, lv2-wp79375-dw02, and rv2-wp79375-dw02, seen in Figure 16a, b, and d, have the lowest decay rate between -140 and -120. These are also the specimens with the least overall mass. Rand-var-03, seen in Figure 16h, has the highest decay rate at the highest level of strain (black) at a value of roughly -400, more than double the decay rate of the lowest mass specimens. Rand-var-03 is also the specimen besides the control with the largest mass. The rand-var specimens, lv2-wp79375-dw06, and rv2-wp79375-dw06 display a higher minimum decay rate than the Uniform, lv2-wp79375-dw02, and rv2-wp-79375-dw02 specimens. The rand-var specimens, lv2-wp79375-dw06, and rv2-wp79375-dw06 have a minimum decay rate of at least -100 while the lower mass specimens have a minimum decay rate near -30. It can be seen that decay rate is not entirely dependent on mass as the control (brown), with the largest mass of the specimens, exhibits a decay rate similar to the third or fourth level of constraint for most of the specimens except rand-var-03.

Overall, the decay rate is determined by both mass and constraint. Decay rate increases with both mass and strain. Therefore, the specimens with the highest damping are the high mass specimens (rand-var, lv2-wp79375-dw06, and rv2-wp79375-dw06) at the highest levels of strain (< 25%). While the control has the largest mass, it is also difficult to constrain and is therefore only tested at 1.8% strain.

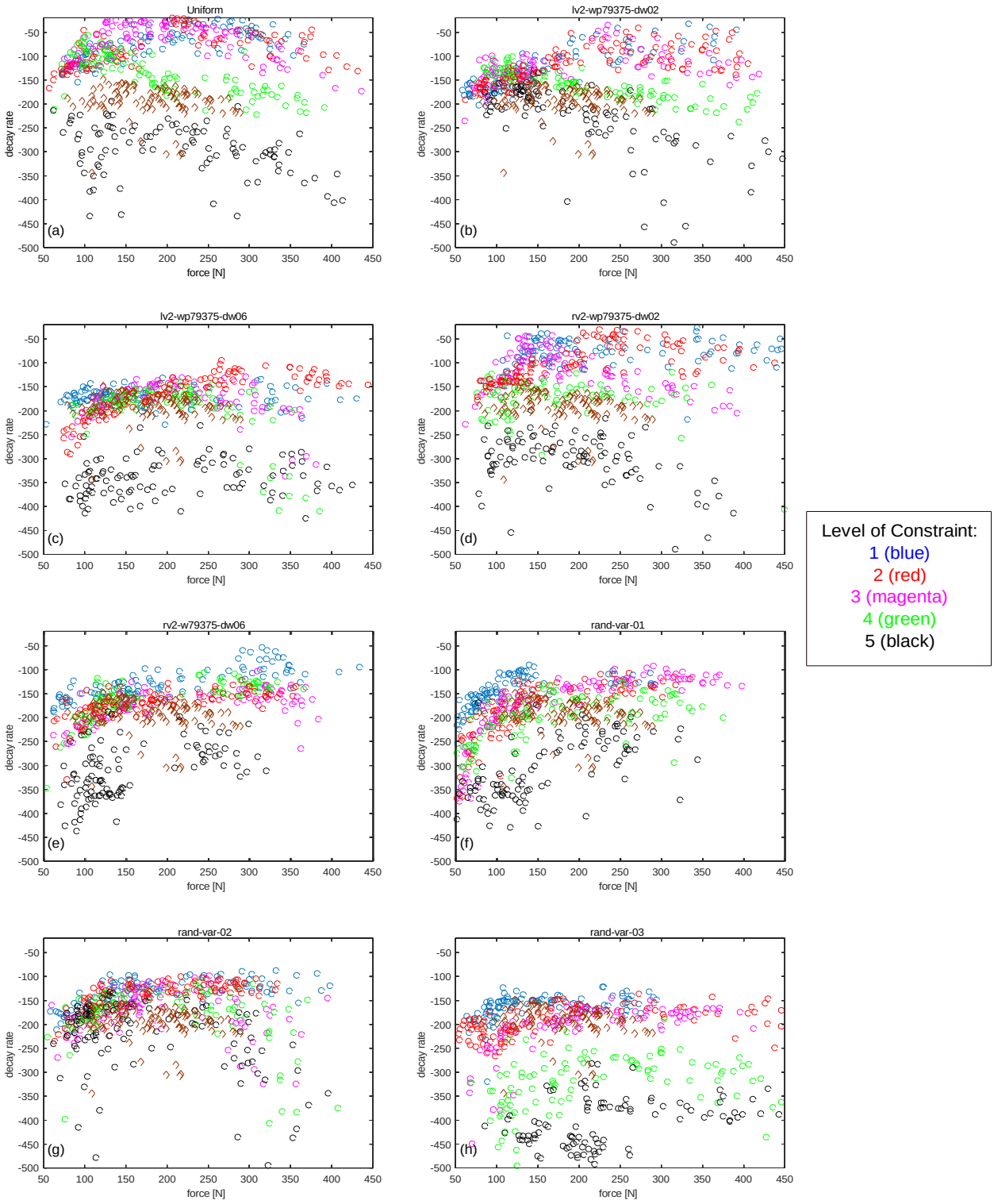

Figure 16: Decay rate as a function of force for the eight specimens in the force transducer output experiment

The levels of constraint (smallest strain to largest) are color coded in the following manner: Blue (first), red (second), magenta (third), green (fourth), and black (fifth). Brown diamonds represent the control specimen values.

Figure 17 examines the force reduction capabilities of the specimens by displaying the peak output force against the input force amplitude for the eight specimens. Each plot contains the force curve for each level of constraint from blue, red, magenta, green, and black for increasing strain and brown for the control values.

All specimens, except control (brown), curves consist of two regions: (1) flat at low input force and (2) linear incline at mid-high input force. The specific range of input force values where these occur depend on both the geometry and the level of constraint. The flat region of the curves can particularly be seen at the first three levels of constraint (blue, red, magenta). The output force for the control (brown) is purely linear and does not show the same trend.

The flat region of the curve is longest for each specimen at the lowest level of constraint (blue). This region shows a constant value of output force regardless of input force. Since this region is not seen in the control (brown), this trend is a property of the hyperdamping material system geometry. This region of constant output force implies a critical input force. Below this boundary input force, a large proportion of the input shock energy is absorbed by the specimen, transmitting a finite output force. This finite output force ranges between 10 N to 25 N, depending on the specimen. The Uniform, lv2-wp79375-dw02, and rv2-wp79375-dw02 specimens, seen in Figure 17a, b, and d, have a lower finite output force closer to 10 N while the remaining specimens have a finite output force closer to 20-25 N.

Table 3: Critical input force for all specimens for first three levels of constraint in force transducer evaluation

	Critical Input Force [N]		
Specimen	First Level (0.5%-6% strain)	Second Level (6%-14% strain)	Third Level (14%-20% strain)
Uniform	212	197	149
lv2-wp79375-dw02	150	143	140
lv2-wp79375-dw06	121	113	110
rv2-wp79375-dw02	205	148	105
rv2-wp79375-dw06	160	107	100
rand-var-01	74	70	79
rand-var-02	104	101	105
rand-var-03	100.5	98	90

Table 3 displays the values for the critical input force for the first three levels of constraint for each specimen. This critical input force is the input force at which the flat region of the curve ends and the linear

incline begins. The Uniform specimen has the largest critical input force at 212 N, followed by the rv2-wp79375-dw02 at 205 N, both at the first level of constraint. The Uniform, lv2, and rv2 specimens show decreasing critical input force with higher strain. Eventually, the critical force decreases enough that the input to output force curve ends it bi-linearity and becomes a linear curve with a single slope. This can especially be seen in the highest level of constraint (black) in Figure 17a. The rand-var specimens have relatively constant values in critical input force across strain.

For the linear incline portion of the curve, seen by every specimen including the control at all levels of constraint, the force reduction of the specimens can be seen by the slope of the curve in that region. A lower value of slope indicates a greater reduction in force. The control (brown) has a slope of 0.36 N/N. In all of the specimens, the slope increases with strain so highest force reduction occurs at low levels of constraint. The lowest values of the slopes are seen in the lv2-wp79375-dw02 and rv2-wp79375-dw02 specimens, (Figure 17b and d) at the first level of constraint (blue) with slopes of 0.13 N/N and 0.15 N/N, respectively. This means that for these linear regions of the curves, only 13% or 15% of the input force is transmitted through the specimen. Other specimens range from slopes of 0.35 N/N to 0.60 N/N for the first level of constraint (blue). Though these values are similar to or higher than the slope of the control (brown), the control does not display the critical input force seen in the other specimens. Yet, the lv2-wp79375-dw02 and rv2-wp79375-dw02 specimens have lower slope values than the control, suggesting that slight changes in beam width from the center allow for greater reduction in force overall under conditions of low strain. Slopes for specimens at higher levels of constraint are generally near a value of 0.60 N/N. This shows that the specimens tend toward a similar overall reduction in force when fully constrained.

In Section 3.1, it is hypothesized that the specimens with slender beams will have the best shock mitigation properties. It can be seen here that this hypothesis is not entirely correct. While the Uniform specimen, which has the most slender beams, does have the largest critical input force, the rv2-wp79375-dw02 specimen (Figure 17d) has both a large boundary input force of 205 N and smaller slope at 0.15 for the first level of constraint (blue). In terms of force reduction, the rv2-wp79375-dw02 specimen is the most ideal of the specimens.

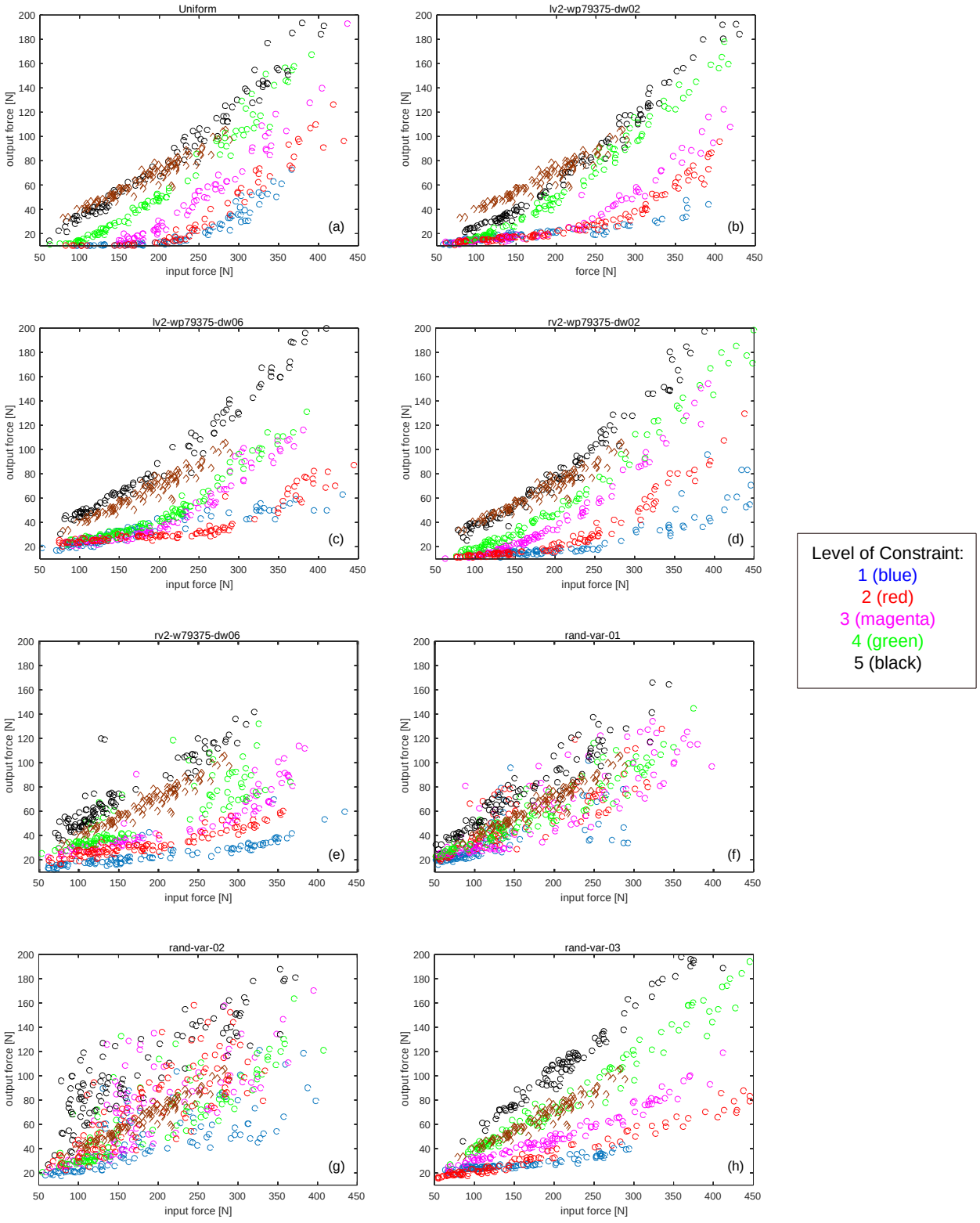

Figure 17: Output force as a function of input force for the eight specimens in the force transducer output experiment

The levels of constraint (smallest strain to largest) are color coded in the following manner: Blue (first), red (second), magenta (third), green (fourth), and black (fifth). Brown diamonds represent the control specimen values.

The mean decay rate as a function of strain is considered in Figure 18 for all of the specimens. Figure 18a compares the decay rate for the Uniform (blue), lv2-wp79375-dw02 (red), and lv2-wp79375-dw06 (green) specimens. All three specimens' curves show increases in decay rate with increasing strain. The Uniform specimen shows the widest range of decay rate values from roughly -80 at the lowest strain (~3%) to -350 at the highest strain (~33%). It also has the lowest decay rate of all the specimens, at a value of roughly -350 at the highest strain. The lv2-wp79375-dw02 specimen starts at a decay rate value of roughly -120 at low strain and increases to a value of -300 at high strain. The lv2-wp79375-dw06 specimen has a relatively flat decay rate curve, starting near -175 at low strain, dipping down to -210 at mid-strain values, then returning back to a decay rate near -175 at high strain.

Figure 18b compares the mean decay rate for the Uniform (blue), rv2-wp79375-dw02 (red), and rv2-wp79375-dw06 (green) specimens. Similarly to the trends of Figure 18a, the decay rate increases with strain. Here, the rv2-wp79375-dw02 specimen increases from -75 at low strain to -275 at high strain. The rv2-wp79375-dw06 specimen increases from -140 at low strain to -220 at high strain.

The mean decay rate for Uniform (blue), rand-var-01 (red), rand-var-02 (green), and rand-var-03 (magenta) specimens is shown in Figure 18c. The rand-var specimens all show similar values in decay rate between -225 and -125. Interestingly, these values also correspond well to the trends seen for the lv2-wp79375-dw06 and rv2-wp79375-dw06 specimens. It is expected that the lv2-wp79375-dw06 specimen acts similarly to the rand-var specimens considering the results of the load frame assessment in Section 4.1, yet in this case, the rv2-wp79375-dw06 specimen also fits well with this trend. The control also had a decay rate at the mid-range value of -200 at a strain of 1.8%. It is likely that at some point in increasing mass within the geometry, mass begins to dominate the determination of the decay rate. Yet, for lower mass specimens, decay rate is more dependent on constraint.

Compared to the decay rate range values seen in the other specimens, the rand-var specimens start with higher decay rate values at the lowest level of constraint. In these three specimens, the mean decay rate is initially -140 while the other specimens generally start around -100. The lv2-wp79375-dw06 and rv2-wp79375-dw06 are exceptions to these cases. Both of these specimens are initially at decay rates of values greater -130. These specimens with starting decay rates greater than the others are also specimens with larger mass, i.e. the rand-var and dw06 specimens. The slightly larger masses of these specimens give the slight advantage in damping at low levels of constraint. Overall, the Uniform still has the largest decay rate across the levels of strain despite having the smallest mass. The damping of the material structure under constraint provides more damping than would otherwise be given from mass alone. This is evidence that hyperdamping material systems at the scale required for shock absorbers can still provide necessary damping beyond that of its elastomer material.

The faster decay of the impulse response at higher levels of strain indicates that these geometries in post-buckled conditions are able to quickly stop impact forces. Yet, as seen from the input to output force amplitude plots, they are not able to reduce the force of the impact to the same extent as when the specimens are in conditions of low strain.

The standard deviation of the decay rate values for each specimen at each level of constraint can be seen in the vertical lines along the decay rate curves. The specimens show a similar range of standard deviation values between 100 and 300. The Uniform, lv2-wp79375-dw02, rv2-wp79375-dw02, and rv2-wp79375-dw06 specimens generally show increased standard deviation at higher levels of strain. The rand-var specimens and lv2-wp79375-dw06 specimens do not show a specific trend of standard deviation with increasing strain.

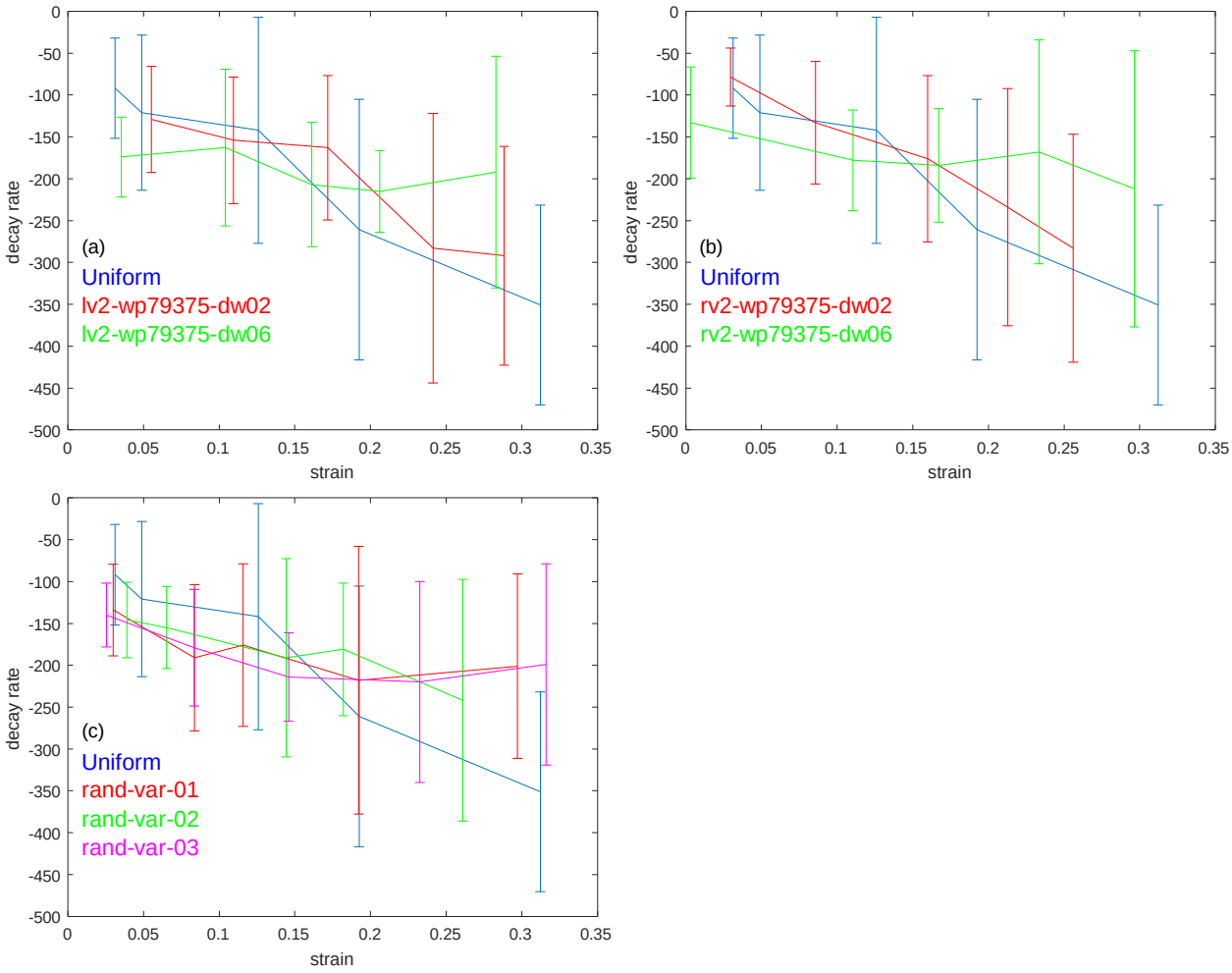

Figure 18: Mean decay rate and standard deviation as a function of strain for the force transducer output experiment (a) Uniform (blue), lv2-wp79375-dw02 (red), and lv2-wp79375-dw06 (green); (b) Uniform (blue), rv2-wp79375-dw02 (red), and rv2-wp79375-dw06 (green); (c) Uniform (blue), rand-var-01 (red), rand-var-02 (green), and rand-var-03 (magenta)

Figure 19 shows the broadband attenuation as a function of strain for the specimens. A larger absolute value of broadband attenuation signifies greater attenuation of the input force by the specimen. Broadband attenuation is computed by taking the fast Fourier transform of the time series data and determining the octave band measures. These values are then summed across the frequencies for each level of strain.

Figure 19a compares the broadband attenuation for the Uniform (blue), lv2-wp79375-dw02 (red), and lv2-wp79375-dw06 (green) specimens. All three specimens show a roughly linear decrease in attenuation with

increasing strain. This matches the results seen in the force amplitude plots in Figure 17. There is a greater reduction in force at lower levels of strain. The Uniform specimen has the largest broadband attenuation of -14 dB at 3% strain. At 33% strain, the broadband attenuation for the Uniform decreases to -8 dB. The lv2-wp79375-dw02 specimen starts from -12 dB at 5% strain and decreases to -9 dB at 30% strain. The lv2-wp79375-dw06 specimen decreases from -9.5 dB at 4% strain to -6.5 dB at 27% strain.

The Uniform (blue), rv2-wp79375-dw02 (red), and rv2-wp79375-dw06 (green) specimens are compared in Figure 19b. Once again, the Uniform has the largest broadband attenuation of -14 dB at low strain. All three specimens show decreasing attenuation with strain. The rv2-wp79375-dw02 specimen starts with a broadband attenuation of -13.5 dB at low strain and ends with a value of -7 dB at high strain. The rv2-wp79375-dw06 specimen starts with a broadband attenuation of -12 dB at low strain and decreases to a value of -6 dB at high strain.

Figure 19c compares the broadband attenuation for the Uniform (blue), rand-var-01 (red), rand-var-02 (green), and rand-var-03 (magenta) specimens. These specimens still exhibit the trend of decreased attenuation at higher strain, with an approximately linear relationship. The rand-var specimens display very similar results, ranging from -10 dB at 3% strain to -6.5 dB at 33% strain, with all three specimens overlapping within that area. The lv2-wp79375-dw06 specimen also overlaps well with the rand-var results.

Comparing the results from all three plots, the broadband attenuation decreases with beam thickness as well as strain. The curves have lower broadband attenuation as beam width increases, which can especially be seen in Figure 19b. Each specimen shows a drop in attenuation of 2 dB to 2.5 dB with 10% increase in strain. These results show that having slender beams at a lower level of strain (0.5% to 6%) causes the greatest reduction in impact force.

Of all eight specimens, the Uniform has the best overall broadband attenuation, agreeing with the hypothesis in Section 3.1. The expectation that the greatest force reduction would occur at near buckling (near the second or third level of constraint) is not met. Instead, highest attenuation for all specimens is consistently at the lowest level of strain. This is possibly due to impact of the hammer on the constrained specimen assembly. Since the bottom of the assembly is fixed in place, the hammer impact causes increased strain on the specimen. This can lead to the specimen buckling even when it is not buckled from the pre-impact constraint set by the two aluminum plates. Thus, the shock of the impact is absorbed by the buckling phenomena that occurs due to the impact.

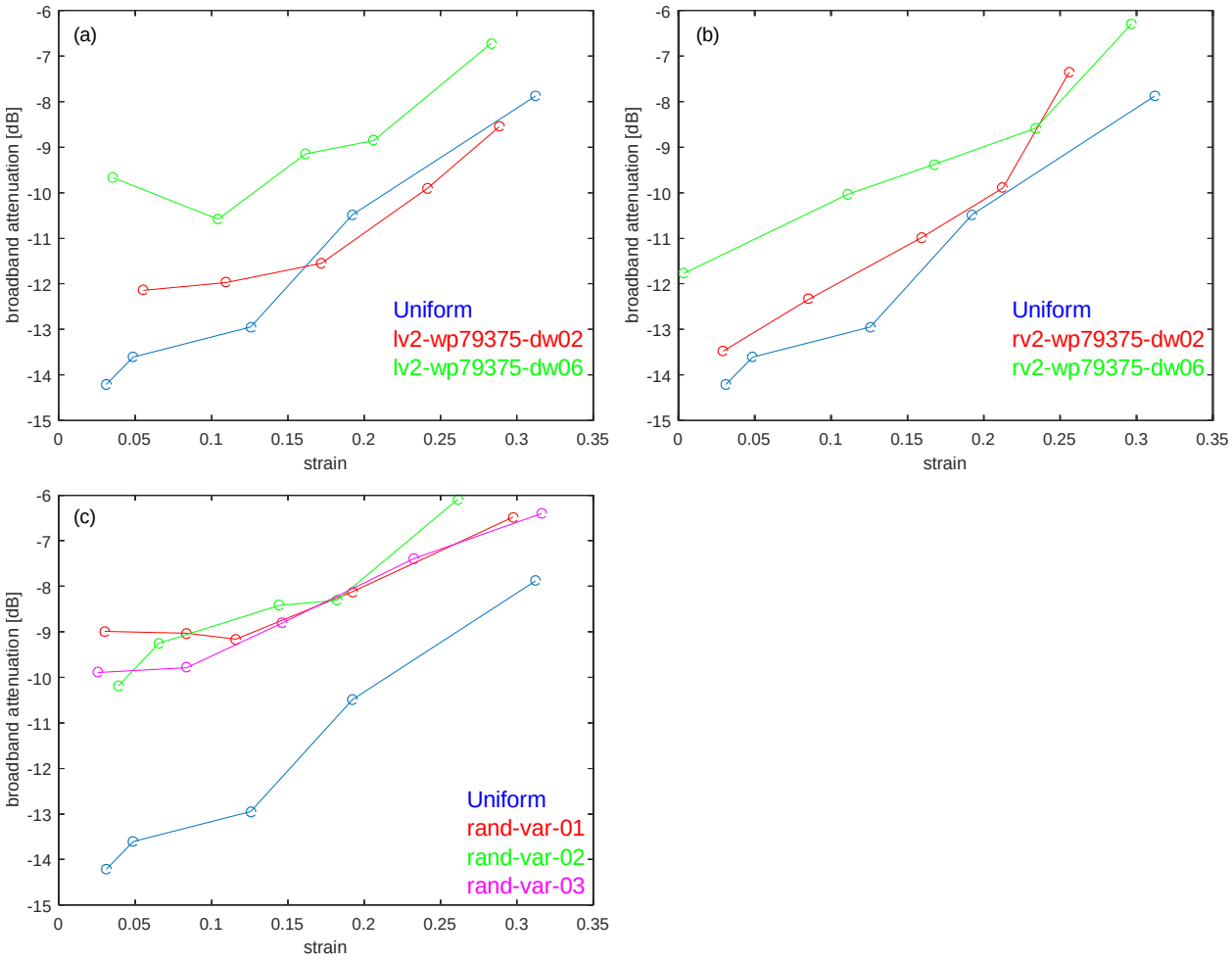

Figure 19: Broadband attenuation of the eight specimens in the force transducer output experiment (a) Uniform (blue), lv2-wp79375-dw02 (red), and lv2-wp79375-dw06 (green); (b) Uniform (blue), rv2-wp79375-dw02 (red), and rv2-wp79375-dw06 (green); (c) Uniform (blue), rand-var-01 (red), rand-var-02 (green), and rand-var-03 (magenta)

4.3 Impact hammer and mini accelerometer results

The peak acceleration experienced during an impact event is an important factor in the causes of traumatic brain injury [8]. The second experimental setup assesses the peak accelerations transmitted through the specimens during impact.

The second experimental setup is evaluated similarly to that of the first setup. The decay rate and peak acceleration magnitudes are used to assess the capability of the specimen designs and compare to results from the first experiment if possible.

Figure 20 displays the decay rate and output acceleration as a function input force for the control specimen. The decay rate has considerable spread in the ranges of decay rate at a given input force. This spread in data is expected due to increased motion involved with the experimental setup. The free movement of the specimen upon impact increases the inherent variability of the data.

It can be seen that the decay rate of acceleration is much higher than the decay rate of force. In Section 4.2, the decay rate value for the control is approximately -200. Here, the decay rate is approximately -1400.

The output acceleration to input force plot shown on the right displays a linear relationship. For the control, the slope of the curve is approximately 0.27 m/s^2-N. The output acceleration ranges from 15 m/s^2 to 130 m/s^2 for an input force range of 100 N to 450 N.

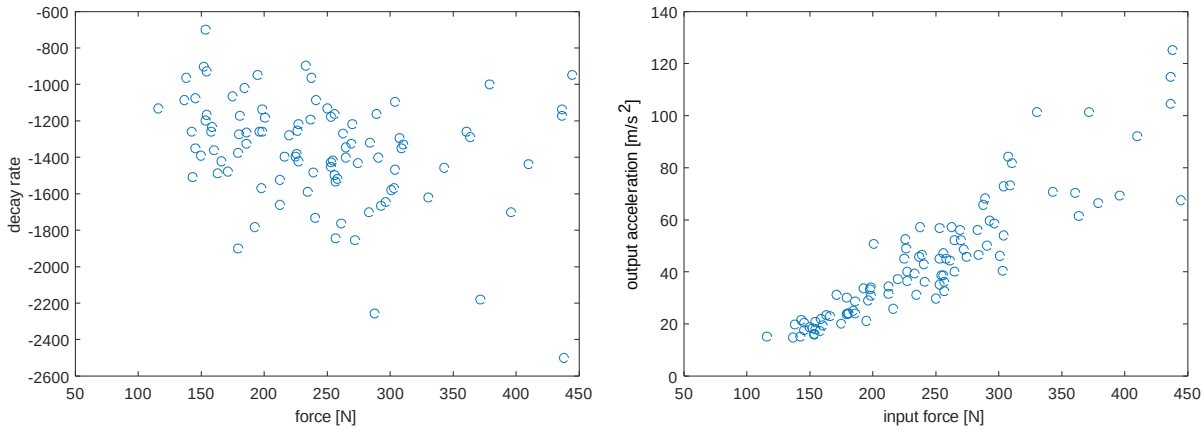

Figure 20: Decay rate (left) and output acceleration (right) as a function of input force for the control specimen in the accelerometer output experiment

The decay rates as a function of input force for the rest of the specimens can be seen in Figure 21. The different colors in each plot correspond to different levels of constraint for each specimen. The colors represent the constraint levels as follows: blue (first), red (second), magenta (third), green (fourth), and black (fifth) with higher levels of constraint corresponding to higher values of strain. The control values are not represented on these plots due to the considerably larger decay rate values of the control. The same trend found in the first experiment in Section 4.2 is also found here, with the curve representing an arch. There is more spread in the decay rate values at low input forces than for the first experiment, and the values for decay rate are much higher due to the increased motion involved with the experimental setup. The decay rate still has less spread and lower value in the middle region (~ 150 N to 300 N) of the input force ranges.

The majority of the decay rates range between -700 and -100. There does not seem to be considerable influence of constraint upon decay rate, though this is discussed in more detail later in this section. The decay rate range for acceleration is much larger than for the force. The decay rate range for force is between -500 and -30. The implications of these results are that hyperdamping protective materials have powerful damping in regards to acceleration.

Similarly to what is seen in Section 4.2, the specimens with the larger masses (rand-var and dw06's) have greater initial decay rates. In this experiment, the control has a significantly higher decay rate, at approximately -1400, than the remaining specimens. This is also likely due to the heavier mass of the control comparatively to the other specimens.

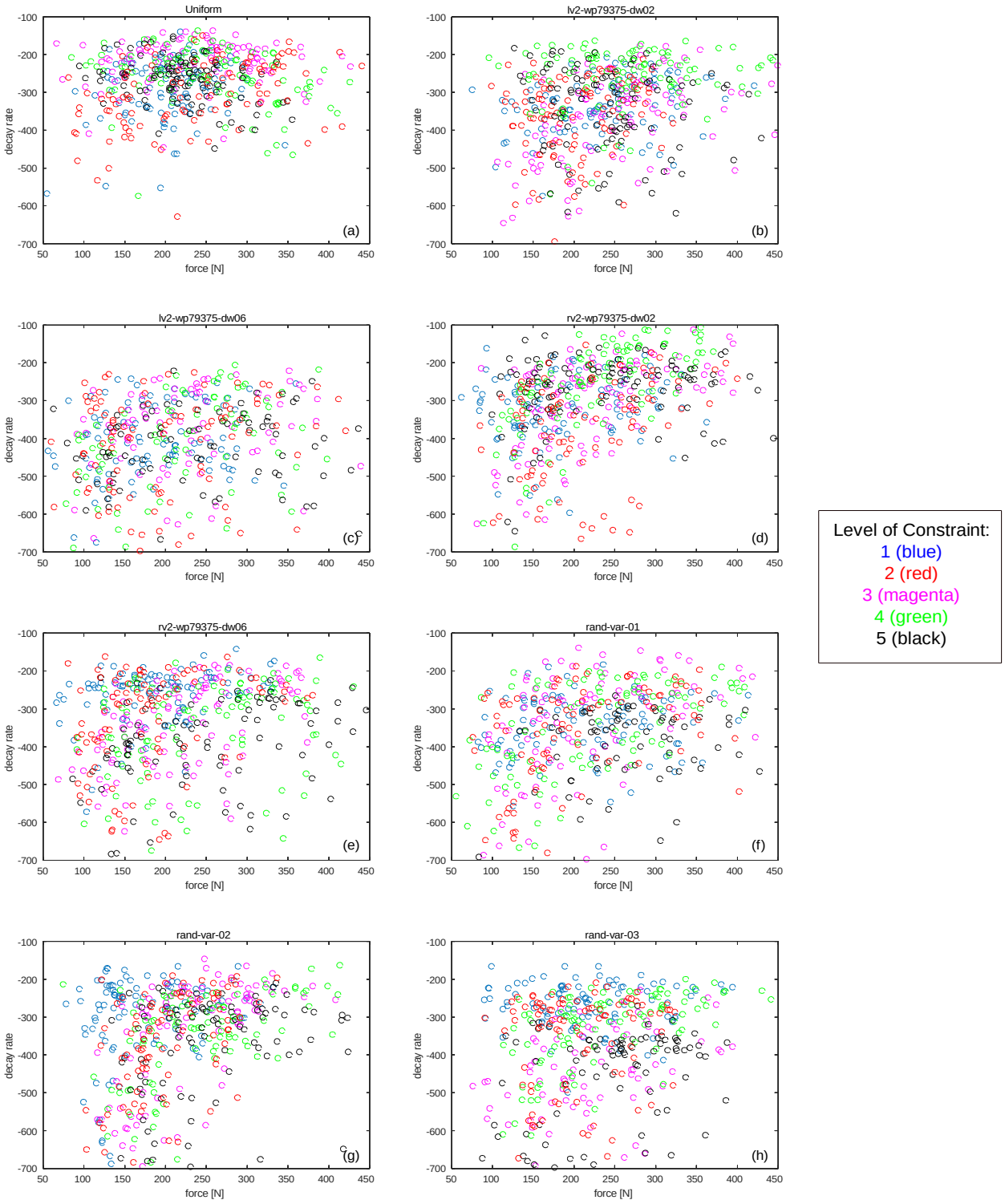

Figure 21: Decay rate as a function of force for the eight specimens in the accelerometer output experiment

The levels of constraint (smallest strain to largest) are color coded in the following manner: Blue (first), red (second), magenta (third), green (fourth), and black (fifth).

There is also much more spread in the accelerometer output data in this experiment than in the force transducer experiment, as seen from Figure 22. Figure 22 displays the output acceleration through each specimen as a function of input force. In each plot, each level of constraint for the specimen is color-coded. The first through fifth levels of constraint are coded as blue, red, magenta, green, and black, respectively. Increasing level of constraint corresponds to increased strain.

The general linear trend is noticeable in the relationship between peak acceleration and input force. The slope of the curve can characterize the relationship between the peak acceleration and input force. A lower slope corresponds to higher acceleration reduction while a steeper slope has less reduction in acceleration for a given input force. The peak acceleration for the specimens generally range from 3 m/s^2 to 20 m/s^2. The specimens with the thinner beams, Uniform, lv2-wp79375-dw02, and rv2-wp79375-dw02 (Figure 22a, b, and d), have the lowest acceleration outputs of the specimens. The Uniform specimen has a slope of approximately 0.02 m/s^2-N. The steepest slope is seen by rand-var-03 (Figure 22h) at approximately 0.06 m/s^2-N.

There is a small change in slope associated with change in constraint. Overall, increasing strain causes a steeper slope. The output acceleration for a given input force is smaller for a lower level of constraint. The change in slope due to increase in strain is slight, with the acceleration not exceeding 8 m/s^2 more than the acceleration at the smallest strain for a given force input.

From these results, it can be seen that the specimens with more slender beams are better at reducing acceleration, agreeing with the hypothesis made in Section 3.1. Of the three specimens with thinnest beams, the Uniform specimen (Figure 22a) reduces acceleration the most and has the lowest slope.

There is a significant difference between the peak acceleration ranges recorded for the specimens and the speak acceleration ranges recorded for the control (~ 10 m/s^2 to 120 m/s^2). This difference can be seen in Figure 23, which displays the peak acceleration as a function of output force for all the specimens at less than 6% strain (first level of constraint) including the control. The control (red) has peak acceleration values that are so significantly higher than the other specimens that the slight differences in acceleration reduction between the other specimens is lost in the comparison. This can be seen in the overlap of the other specimen curves at the bottom of the plot.

There is a maximum 93% reduction in output acceleration for the Uniform at the lowest level of strain from the control. The capability of the specimens to absorb impact energy is seen from this difference, especially when comparing the mass of the control to the mass of specimens. The specimens are able to significantly reduce the peak acceleration due to the impact event at less than three-fourths the mass of the solid elastomer control.

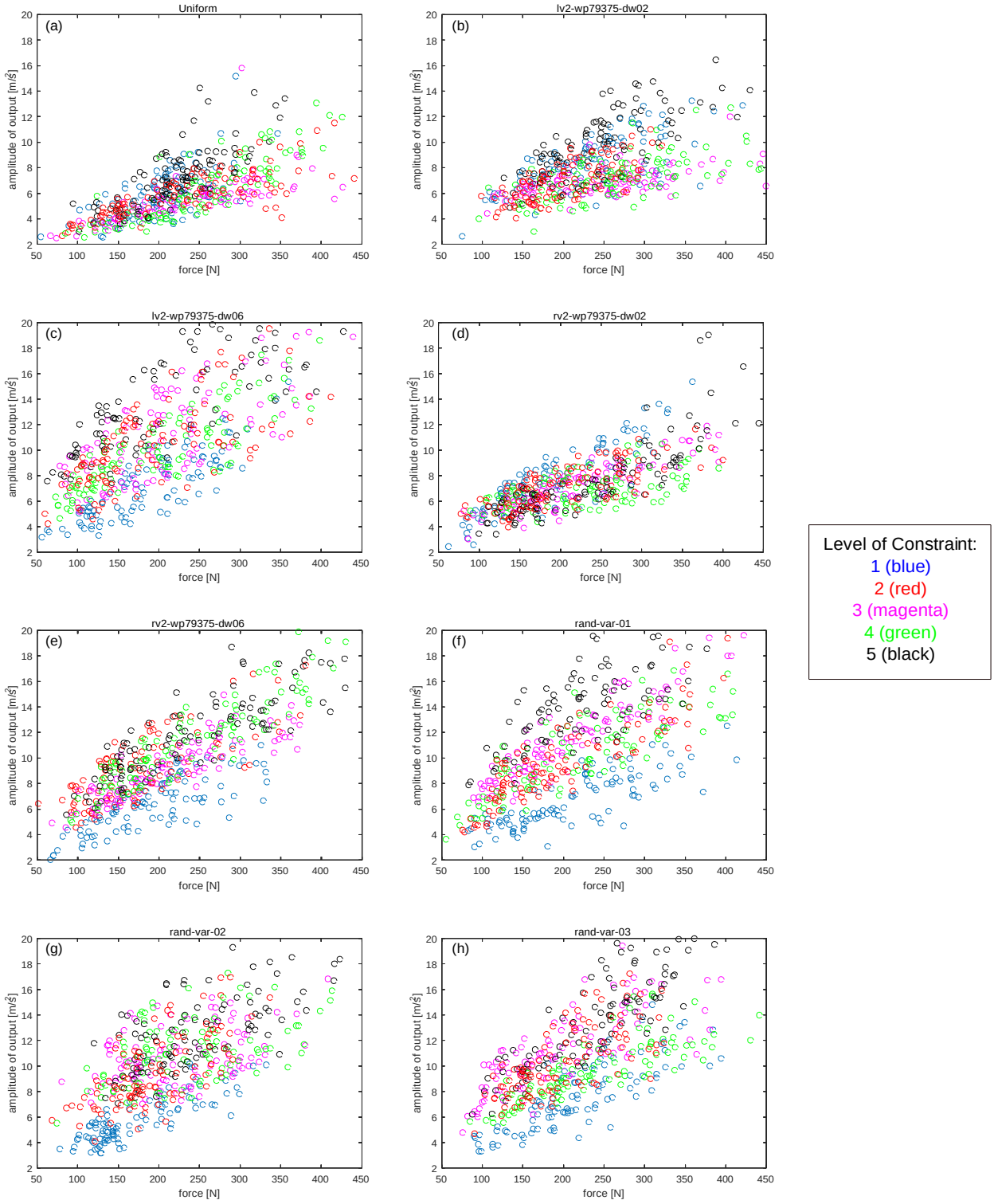

Figure 22: Output acceleration as a function of input force for the eight specimens in the accelerometer output experiment

The levels of constraint (smallest strain to largest) are color coded in the following manner: Blue (first), red (second), magenta (third), green (fourth), and black (fifth).

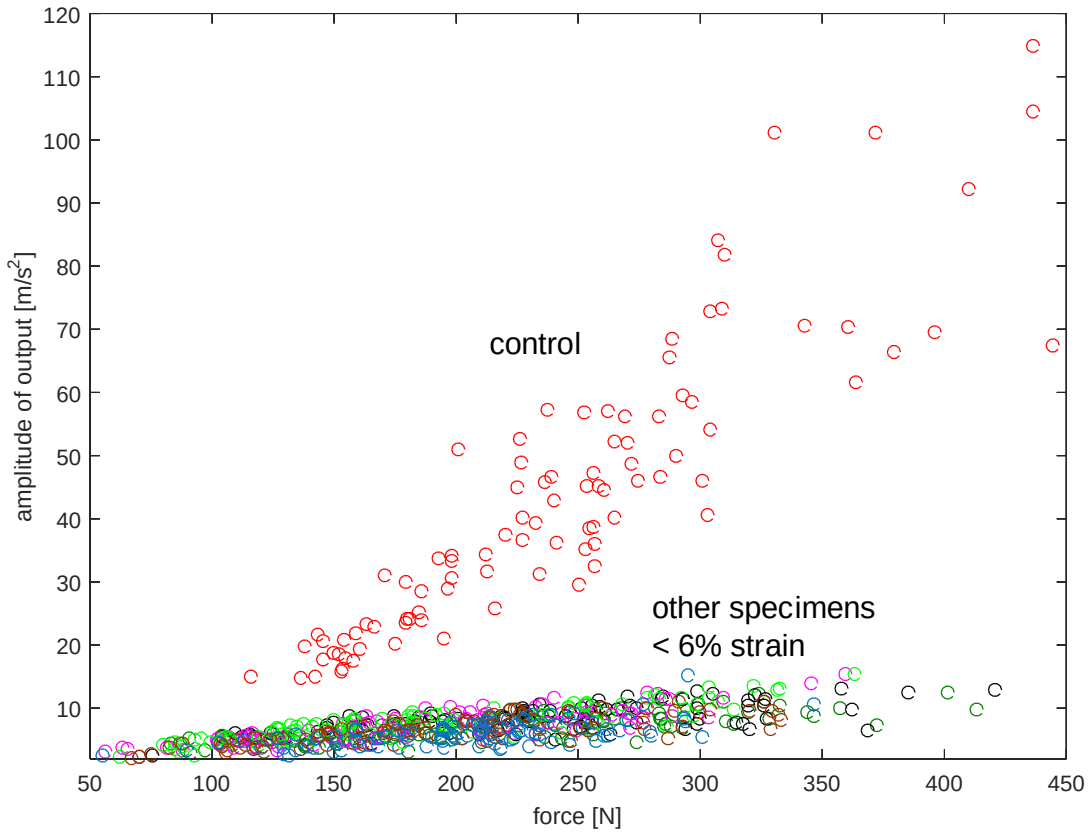

Figure 23: Output peak acceleration as a function of input force for the control (red) and other specimens at the first level of constraint

Figure 24 shows the mean decay rate as a function of strain for each specimen in the accelerometer evaluation. Figure 24a compares the Uniform (blue), lv2-wp79375-dw02 (red), and lv2-wp79375-dw06 (green) specimens. The lv2-wp79375-dw06 specimen has the greatest decay rate, varying from -425 at 4% strain to -600 at 13% strain. The Uniform specimen has the lowest decay rate varying from -275 at 2% strain to -220 at 15% strain.

In Figure 24b, the Uniform (blue), rv2-wp79375-dw02 (red), and rv2-wp79375-dw06 (green) specimens are compared. Here, the rv2-wp79375-dw06 specimen has the greatest decay rate of -450 near 26% strain. The Uniform once again has the lowest decay rate value of -220 at 15% strain.

The Uniform (blue), rand-var-01 (red), rand-var-02 (green), and rand-var-03 (magenta) specimens are compared for decay rate in Figure 24c. As seen from the decay rate plots in Figure 18 in Section 4.2, the rand-var specimens still behave very similarly to one another, though there is more variation in decay rate values for the accelerometer evaluation results. The rand-var-01 and rand-var-03 specimens have the largest decay rate of the four with a value of -625 at 27% strain for the rand-var-01 and a value of -615 at 12% strain for the rand-var-03.

Overall, there is an increase in decay rate with increasing mass. The masses of each specimen can be found in Table 2. The Uniform specimen has the lowest mass at roughly 10 g, while the rand-var-03 specimen

has the highest mass (excluding control) at approximately 12.5 g. The lv2-wp79375-dw06, rv2-wp79375-dw06, and rand-var specimens have the largest decay rate values as well as he largest masses. Considering the significantly decay rate values of the control (~ -1400), this larger decay rate is likely entirely a consequence of mass.

The standard deviation for each specimen can be seen in the vertical lines extending from the decay rate curves at each level of constraint. Standard deviation increases with mass. This trend can be seen especially well in Figure 24a, where the Uniform (blue) has the shortest vertical lines, and thus standard deviation, and the lv2-wp79375-dw06 (green) has the longest.

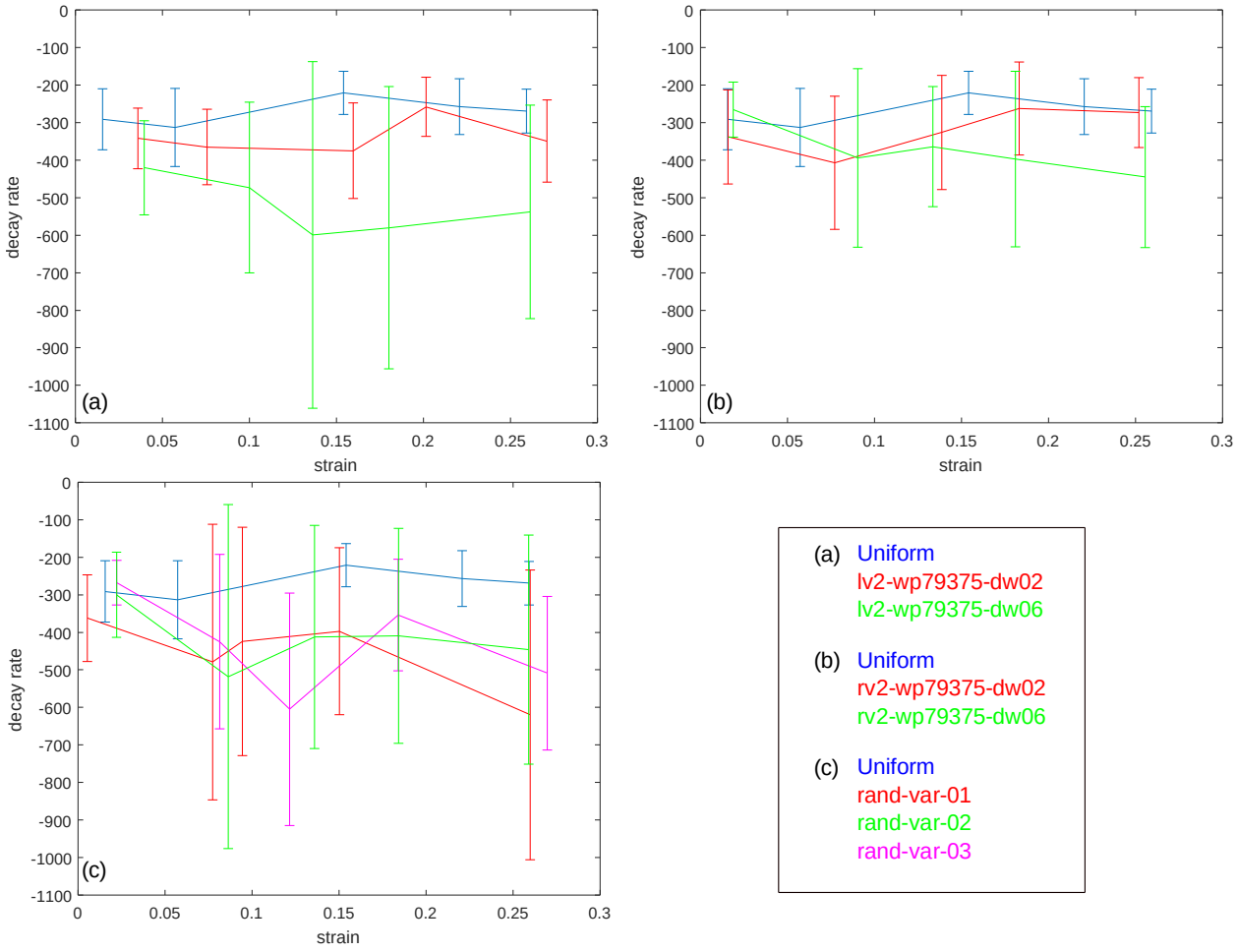

Figure 24: Mean decay rate and standard deviation as a function of strain for the accelerometer output experiment (a) Uniform (blue), lv2-wp79375-dw02 (red), and lv2-wp79375-dw06 (green); (b) Uniform (blue), rv2-wp79375-dw02 (red), and rv2-wp79375-dw06 (green); (c) Uniform (blue), rand-var-01 (red), rand-var-02 (green), and rand-var-03 (magenta)

The broadband attenuation as a function of strain for this experiment can be seen in Figure 25. Unlike with the results of the first experiment from Section 4.2, there is no steady downward decline of broadband attenuation with an increase in strain.

Figure 25a compares the broadband attenuation for the Uniform (blue), lv2-wp79375-dw02 (red), and lv2-wp79375-dw06 (green) specimens. The Uniform and lv2-wp79375-dw02 specimens have the greatest

attenuation of -20.5 dB at 15% strain and 22% strain, respectively. Of them all, the Uniform specimen shows greater attenuation of acceleration over the range of strain values. The lv2-wp79375-dw06 specimen has the lowest attenuation at a value of -16.75 dB at 27% strain.

Figure 25b compares the attenuation of the Uniform (blue), rv2-wp79375-dw02 (red), and rv2-wp79375-dw06 (green) specimens. Once again, the Uniform has the greatest attenuation in acceleration at a value of -20.5 dB at roughly 15% strain. The rv2-wp79375-dw06 specimen has the lowest attenuation of -17 dB at 9% strain.

In Figure 25c, the Uniform (blue), rand-var-01 (red), rand-var-02 (green), and rand-var-03 (magenta) specimens are compared for broadband attenuation. The rand-var specimens all compare similarly with considerable overlap between them. The Uniform specimen has the largest broadband attenuation while rand-var-01 has the smallest of -16.5 dB at 26% strain. The lv2-wp79375-dw06 specimen also matches closely the rand-var specimen trends.

There are also correlations between the broadband attenuation results in Figure 25 and the mean decay rate plots in Figure 24. Where there are local minimums in the broadband attenuation plots, there are local maximums in the mean decay rate plots. Since ideal specimens have large values for both broadband attenuation and mean decay rate, it's likely that a middle ground for constraint level will have to be determined when designing for optimal broadband attenuation and decay rate in future specimens.

Overall, there is a larger broadband attenuation for specimens with thinner beams, i.e. the Uniform and dw02 specimens. This matches the results of the force attenuation seen in Section 4.2. These specimens display a higher capacity for impact attenuation despite having lower masses than the remaining specimens. In other words, hyperdamping material system specimens with thinner beams are more effective at reducing shock energies of impact than specimens with wider beams, even considering the smaller mass that constitutes the specimens with thinner beams.

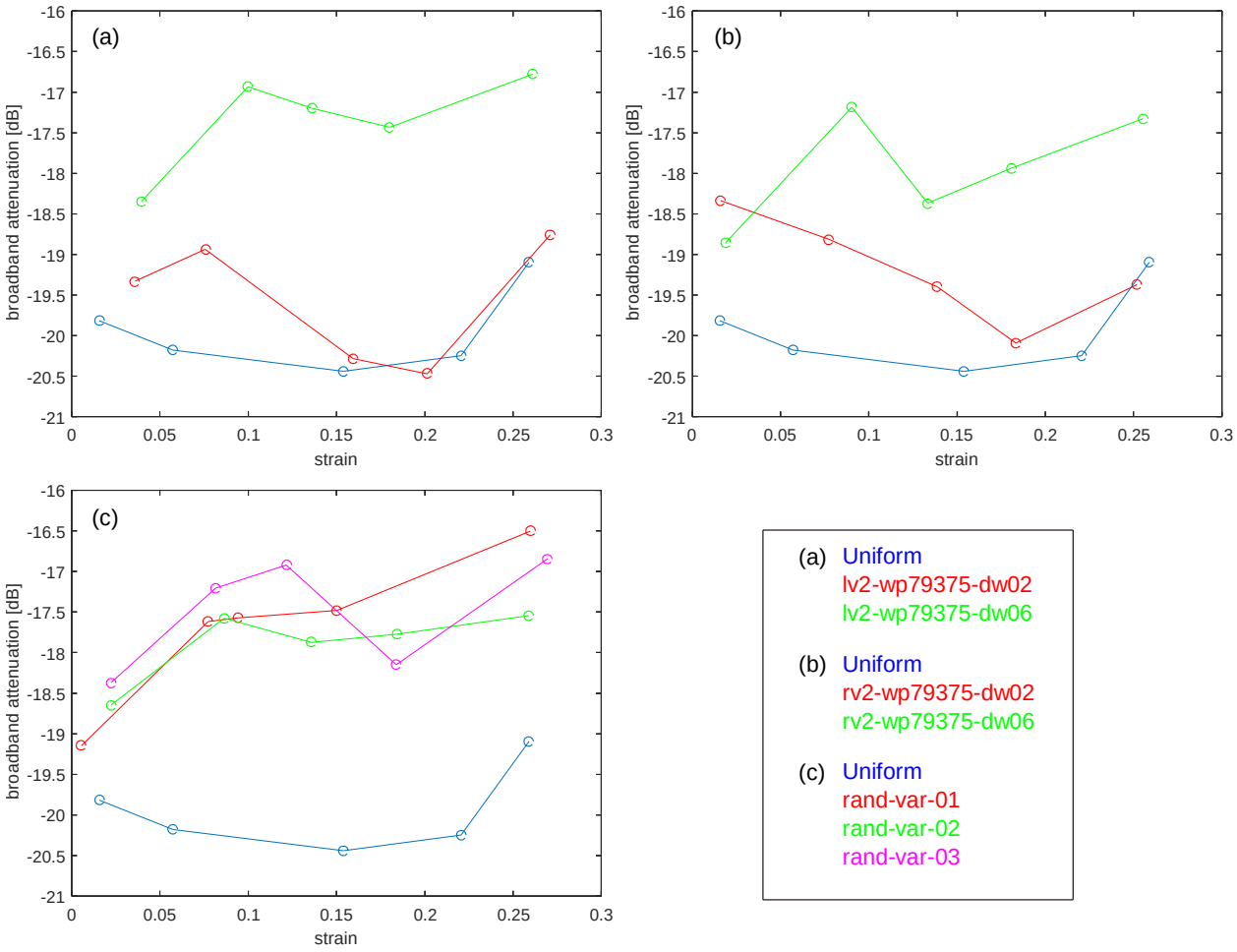

Figure 25: Broadband attenuation of the eight specimens in the accelerometer output experiment (a) Uniform (blue), lv2-wp79375-dw02 (red), and lv2-wp79375-dw06 (green); (b) Uniform (blue), rv2-wp79375-dw02 (red), and rv2-wp79375-dw06 (green); (c) Uniform (blue), rand-var-01 (red), rand-var-02 (green), and rand-var-03 (magenta)

5 CONCLUSION

Helmets are commonly used protective devices known for their widespread use in both industrial and sports-related capacities. Despite this, common helmet liners do not provide adequate impact shock absorption. Users still carry a considerable risk for concussions and traumatic brain injuries even when wearing helmets. Common helmet liners such as EPS foam rely on mass to attenuate force upon impact. Such helmet designs require large quantities of both stiff and resilient foam liners to not only absorb impact, but also adjust to the contour of the user's head to avoid helmet roll-off. Requiring multiple types of foam inside a helmet increases both the weight and volume of the design without improving helmet performance.

Hyperdamping material designs focus on ideas of material design and mechanical properties of beams to absorb substantial wave and vibration energy with little mass. By constraining the elastomer beams within the design, it is possible to nullify the natural frequency and therefore provide substantial damping.

This research explores the suitability of hyperdamping protective material systems as lightweight shock absorbers. Computational models are used to determine key parameter ranges within the geometries while allowing simple models to inspire specimen designs for testing. Experimental setups evaluate the capacity of the specimens to reduce force and acceleration upon impact at various levels of constraint, from unbuckled to severely buckled. The results are assessed through direct input to output force amplitude, input to output peak acceleration, decay rate as a function of strain, and broadband attenuation.

The computational model results indicate that designs with overall smaller beam widths have a higher capacity for force reduction/energy absorption as they have a lower natural frequency than designs with larger beam widths at a given level of constraint. This agrees with the majority of the results from the experimental studies, where the designs with smallest beam widths perform usually better than, or at least on level with, specimens of larger beam thicknesses in input to output force amplitude and input to output peak acceleration. The control specimen, a solid mass of elastomer, has not performed on par with the other eight specimens. This development is quite significant when considering that the specimens are outperforming the control at only 60-75% of the control's mass.

Most significantly, the specimens are able to substantially reduce acceleration upon impact. When compared to the peak acceleration values for the control, the specimens have as much as a 93% reduction in acceleration.

The force reduction capacity for many of the specimens is also of great advantage in that the specimens display an ability to output a finite force independent of impact force up to a certain critical force input. The critical input force up to which the specimens absorb is determined by the level of constraint and geometry, with specimens under lower levels of strain showing increased absorption.

The results found in this research strongly suggest that hyperdamping material systems are a viable solution for maintaining shock absorption while decreasing mass and weight within helmet designs and other protective equipment. Yet, this research is only an introduction to the possibility of hyperdamping protective material systems and their advantages. Moving forward, there are several means by which this

research can be further augmented. The specimen designs assessed within this research are simple and meant for quick evaluation of the properties. A more thorough study into the designs, such as looking at the effect of number of stages or number of beams across a stage, could determine a design far more capable than the ones presented here. While this study examines the specimens' ability to reduce linear acceleration, rotational acceleration is also an important factor in causing concussions [8] and should be investigated in further impact studies. Additionally, efforts into implementing designs easily within traditional helmets and assessing designs in environments that more closely resemble that of a helmet shock absorber would provide considerable means towards the use of hyperdamping material systems within helmet designs.

BIBLIOGRAPHY

[1] Brain Injury Association of America, "About Brain Injury," Brain Injury Association of America, 2015. [Online]. Available: http://www.biausa.org/about-brain-injury.htm. [Accessed 25 March 2017].

[2] M. Marar, N. McIlvain, S. Fields and C. R.D., "Epidemiology of Concussions Among United States High School Athletes in 20 Sports," *The American Journal of Sports Medicine*, pp. 747-755, 2012.

[3] "Most concussions deliver 95 g's, neuropsychologist says," ScienceDaily, 25 June 2010. [Online]. Available: https://www.sciencedaily.com/releases/2010/06/100624092526.htm. [Accessed 20 March 2017].

[4] R. Wrona, "The use of state workers' compensation administrative data to identify injury scenarios and quantify costs of work-related traumatic brain injuries," *Journal of Safety Research*, pp. 75-81, 2006.

[5] D. Meaney and D. Smith, "Biomechanics of Concussion," *Clinics in Sports Medicine*, vol. 30, no. 1, pp. 19-31, 2011.

[6] J. Swearingen, "Tolerances of the Human Brain to Concussion," FAA Civil Aeromedical Institute, Oklahoma City, 1971.

[7] J. Gever, "Any Football Helmet Hit Can Cause Potential Concussion," MedPage Today, 07 December 2007. [Online]. Available: http://www.medpagetoday.com/neurology/generalneurology/7625. [Accessed 22 March 2017].

[8] J. Barth, J. Freeman, D. Broshek and R. Varney, "Acceleration-Deceleration Sport-Related Concussion: The Gravity of It All," *Journal of Athletic Training*, vol. 36, no. 3, pp. 253-256, 2001.

[9] J. Eckner, M. Sabin, J. Kutcher and S. Broglio, "No Evidence for Cumulative Impact Effect on Concussion Injury Threshold," *Journal of Neurotrauma*, vol. 10, pp. 2079-2090, 2011.

[10] K. Guskiewicz, M. McCrea and S. Marshall, "Cumulative Effects Associated With Recurrent Concussion in Collegiate Football Players," *Journal of American Medical Association*, vol. 290, no. 19, pp. 2549-2555, 2003.

[11] F. Shuaeib, A. Hamouda, S. Wong, R. Umar and M. Ahmed, "A new motorcycle helmet liner material: The finite element simulation and design of experiment optimization," *Materials & Design*, pp. 182-195, 2007.

[12] N. Mills and A. Gilchrist, "Bicycle helmet design," *Proceedings of the Institution of Mechanical Engineers, Part L: Journal of Material Design and Applications,* pp. 167-180, 2006.

[13] Xenith, "The Xenith Difference," 2017. [Online]. Available: https://www.xenith.com/pages/xenith-technology. [Accessed 25 March 2017].

[14] R. Stella, "Flexible Football Helmet Absorbs Hits Like A Car Bumper, Could Put An End To Concussions," Digital Trends, 13 January 2016. [Online]. Available: http://www.digitaltrends.com/cool-tech/zero-1-football-helmet-helps-prevent-concussions/. [Accessed 14 July 2016].

[15] 6D Helmets, "Omni-Directional Suspension Technology - Exclusive in 6D Helmets," 6D Helmets, 2017. [Online]. Available: http://www.6dhelmets.com/innovation/#AAE. [Accessed 14 July 2016].

[16] A. Rafsanjani, A. Akbarzadeh and D. Pasini, "Snapping Mechanical Metamaterials under Tension," *Advanced Materials,* vol. 27, no. 39, pp. 5931-5935, 2015.

[17] S. Shan, S. Kang, J. Raney, P. Wang, L. Fang, F. Candido, J. Lewis and K. Bertoldi, "Multistable Architected Materials for Trapping Elastic Strain Energy," *Advanced Materials,* pp. 4926-4301, 2015.

[18] B. Florijn, C. C. and M. van Hecke, "Programmable Mechanical Metamaterials," *Physical Review Letters,* vol. 113, no. 17, p. 175503, 2014.

[19] R. L. Harne, Y. Song and Q. Dai, "Trapping and attenuating broadband vibroacoustic energy with hyperdamping metamaterials," *Extreme Mechanics Letters,* vol. 12, pp. 41-47, 2017.

[20] T. Proctor and F. Rowland, "Developments of Standards for Industrial Safety Helmets-The State of the Art," *Journal of Occupational Accidents,* vol. 8, pp. 181-191, 1986.

6 APPENDIX

6.1 Sample MATLAB code for load frame assessment

Below is the sample MATLAB code, using data acquisition toolbox, to acquire and filter data from the load cell and laser displacement sensor used in the load frame assessment of the specimens.

```
%% data acquisition toolbox NI
clear all
warning off

%%
% preset post-processing built for load-frame experiments using load cell
% and displacement transducers

%% acquire data?
dataacquire=1; % yes for acquire

%% experimental setup parameters
d.test_name='load_frame'; % type of excitation delivered to beam

%% test specimen name, parameters
d.specimen='rand-var-03'; % specimen name, or no_specimen if none

%% data acquisition setup parameters
d.fs=256*1; % sampling frequency [Hz]
d.wind=@hann; % window type for averages
d.seconds=310; % [s] seconds of data acquisition, determined according to Vibration Research
VR9500 controller test setup
d.filter_data_lo=35; % [Hz] of low pass cut off frequency

%% filename for save d structure
c=clock; % grab the time-stamp, eliminates possibility of data overwrite
d.filename=[num2str(c(1)) '_' num2str(c(2),'%02.0f') '_' num2str(c(3),'%02.0f') '_'
num2str(c(4),'%02.0f') '_' num2str(c(5),'%02.0f') '_' num2str(c(6),'%02.0f') '_' d.test_name '_'
d.specimen '.mat'];
saveon=1; % save the data?

%% sensor sensitivity
d.sensor{1}='PCB_110205A_SN920_load_cell_and_signal_conditioner_8162011A_SN1273';
d.ch_sens(1)=110/10; % N/V
d.sensor{2}='Micro_epsilon_ILD1700_SN1503086_laser_displacement_sensor';
d.ch_sens(2)=20/1; % mm/V

%% mean sensor values [V] for each channel, to be subtracted from the input before sensitivity to
[units]
d.data_mean(1)=0.563746398356367; %
d.data_mean(2)=5.211900919251564; %

%% if for data acquisition
if dataacquire==1 % 1=yes for acquire

%% identify connected devices
devices=daq.getDevices;
% once obtained, ensure using correct device name in below session and acquire lines

%% acquire data
s=daq.createSession('ni');
s.addAnalogInputChannel('Dev1',11,'Voltage'); % add input channels
s.addAnalogInputChannel('Dev1',12,'Voltage'); % add input channels
s.Rate=d.fs; % set output and measuring frequency [Hz]
s.DurationInSeconds=d.seconds; % [s] duration of data acquisition
[d.data,d.time_series]=s.startForeground;
d.nn_chan=min(size(d.data));

%% bandpass filter data
clear ch_f
d.nn_chan=min(size(d.data));
```

```
myfilt=designfilt('lowpassiir','filterorder',4,'passbandfrequency',d.filter_data_lo,'PassbandRipp
le',0.01,'samplerate',d.fs);
%
myfilt=designfilt('bandpassiir','filterorder',4,'HalfPowerFrequency1',d.filter_data_lo,'HalfPower
Frequency2',d.filter_data_hi,'samplerate',d.fs);
for iii=1:d.nn_chan
ch_f(:,iii)=filtfilt(myfilt,d.ch_sens(iii)*(d.data(:,iii)-d.data_mean(iii))); %
end

%%
end

%% assign filtered data
d.data_filt=ch_f; % re-assign filtered data from local to structure variable

%% plot
colors=['r' 'g' 'b' 'c' 'm'];
markers=['o' 's' 'd' 'v' '^'];
color_plot=2;
smooth_inc=101;

undeformed_thickness=13.05; % [mm] undeformed specimen thickness

figure(1);
% clf;
hold on;
trunc=100:20:round(1*length(d.time_series));
% plot(d.data(trunc,2),-d.data(trunc,1))
plot(1e-0*d.data_filt(trunc,2),smooth(-
d.data_filt(trunc,1),smooth_inc),'color',colors(color_plot))
xlabel('displacement [mm]');
% xlabel('strain');
% xlabel('effective width ratio');
ylabel('force [N]');
box on
title([strrep(d.filename,'_','-')])

figure(2);
% clf;
hold on;
plot(1e-0*d.data_filt(trunc,2),1e-3*gradient(smooth(-
d.data_filt(trunc,1),smooth_inc))./gradient(smooth(1e-
3*d.data_filt(trunc,2),smooth_inc)),'color',colors(color_plot))
xlabel('displacement [mm]');
% xlabel('strain');
% xlabel('effective width ratio');
ylabel('stiffness [kN/m]');
ylim([-5 50]);
box on
title([strrep(d.filename,'_','-')])

%% save data
if saveon==1
    d.data_filt=[];
    save(d.filename,'d');
end

%%
```

6.2 Sample MATLAB code for experimental setup

Below is the sample MATLAB code, using data acquisition toolbox, to acquire and filter data from the impact hammer and mini accelerometer experimental setup. The same code is used for the impact hammer and force transducer setup with minor adjustments. The post-processing of the data is also included within the code.

```
%% data acquisition toolbox NI
```

```
clear all
warning off

%% plot styles
colors=['k' 'r' 'g' 'b' 'm' 'k' 'r' 'g' 'b' 'c' 'm'];
mtypes=['o' 'v' 's' '^' 'd' 'o' 'v' 's' '^' 'x' 'd'];

%% acquire data?
dataacquire=1; % yes for acquire

%% data acquisition setup parameters
d.fs=65536*2; % sampling frequency [Hz]. Chosen so that each impact peak has ~4 data points to
avoid aliasing
d.seconds=2; % [s] seconds of data acquisition

d.filter_data_lo=50; % [Hz] low-pass digital filter frequency
d.filter_data_hi=18000; % [Hz] high-pass digital filter frequency

%% filter create
%
myfilt=designfilt('lowpassiir','filterorder',2,'passbandfrequency',d.filter_data_hi,'PassbandRipp
le',0.01,'samplerate',d.fs);
myfilt=designfilt('bandpassiir','filterorder',2,'HalfPowerFrequency1',d.filter_data_lo,'HalfPower
Frequency2',d.filter_data_hi,'samplerate',d.fs); % filter result

%% parameters for hammer impact
d.numoutputs=1; % number of simultaneous output sensor locations
d.numlocs=1; % number of input locations on beam
d.numhits=100; % target number of(modal hammer impacts) per location
d.threshold_impact_force=40; % [N] any force above this level is flagged as an impact event
d.time_fft=.10; % [s] time to collect data after each impact
d.sec_jump=.01; % TUNABLE PARAMETER [s] seconds to jump forward after each impact registration.
Each impact must occur in less time than this value

%% test specimen name, parameters, filenumber if need more than 1
d.specimen='rand-var-03'; % specimen name, or no_specimen if none
d.constraint_height=0.3455; % [inch] height of constrained/compressed specimen

%% filename for save d structure
c=clock;
d.filename=[num2str(c(1)) '_' num2str(c(2),'%02.0f') '_' num2str(c(3),'%02.0f') '_'
num2str(c(4),'%02.0f') '_' num2str(c(5),'%02.0f') '_' num2str(c(6),'%02.0f') '_hammer_'
d.specimen '_impact.mat'];
fige1='_decay_rate_force.fig';
fige2='_amplitude_input_output.fig';
saveon=1; %overwrite is not possible due to timestamp in filename

%% sensor sensitivity
d.sensor{1}='PCB_086C01_SN37316_force_transducer_impact_hammer';
d.ch_sens(1)=1/0.01108; % N/V
d.sensor{2}='PCB_U352A10_SN4618_mini_accelerometer';
d.ch_sens(2)=16.9600475; % (m/s^2)/V
%d.ch_sens(3)=1/.01*9.81; % N/V

d.nn_chan=length(d.ch_sens);

%% mean sensor values, this only plays a role in determining mean-square responses if relevant
d.data_mean(1)=0; % mean force transducer voltage [V]
for iii=1:d.numoutputs
    d.data_mean(iii+1)=0; % mean accel sensor voltage [V]
end

%% if for data acquisition
if dataacquire==1 % 1=yes for acquire
    %% identify connected devices
    devices=daq.getDevices;
    %once obtained, ensure using correct device name in below session and acquire lines

%% data acquisition setup
s=daq.createSession('ni');
s.addAnalogInputChannel('Dev3',13,'Voltage'); % add input channels
```

```
s.addAnalogInputChannel('Dev3',9,'Voltage'); % add input channels
s.DurationInSeconds=d.seconds; % [s] time for recording
s.Rate=d.fs; % set output and measuring frequency [Hz]

    %% acquire data
    d.hitInd=zeros([d.numlocs d.numhits]);
    pause(2) % provide time for user to move from computer to test station
        for iii=1:d.numlocs
            fprintf('Move to location %i\n', iii);
            % sound
            asdf=linspace(1/8192,1/4,2048);sound([sin(2*pi*1000*asdf)  sin(2*pi*800*asdf)],8192);
% signals user to move on to next location

            pause(1) % pause allows user to move to new location
            jjj=1;
            while jjj<=d.numhits
                % sound
                asdf=linspace(1/8192,1/4,2048);sound(sin(2*pi*800*asdf),8192) % signals user to
hit immediately

                data_ind=jjj+(iii-1)*d.numhits; % integer increasing index to append data to
after data acquisition

                % data acquisition
                [d.data,d.time]=s.startForeground; % collect data for one impact

                d.data_store(:,data_ind,:)=d.data; % append data to stored matrix
                d.time_series(:,data_ind)=d.time; % append timeseries to stored matrix

                hitIndCheck=find(abs(d.ch_sens(1).*d.data(1:end-
d.time_fft*d.fs,1))>d.threshold_impact_force,1,'first'); % check if impact occurred with enough
data after impact for processing
                if isempty(hitIndCheck)
                    % do nothing, repeat this iteration through the loop
                else
                    d.hitInd(iii,jjj)=hitIndCheck; % if hit did occur, append to stored matrix
                    jjj=jjj+1;% if hit did occur, increase counter
                end
                % clear data for next loop
%                 d.data=[];
%                 d.time=[];
                hitIndCheck=[]; % clear data for next loop
            end
        end
%         fprintf('move laser to next location\n')
        % sound
        asdf=linspace(1/8192,1/4,2048);sound([sin(2*pi*1200*asdf)  sin(2*pi*1000*asdf)],8192); %
signals user to move on to next location

%         pause % pause until user input to allow for laser to be moved
%         pause(1)
end
%% take FFT of data
samples_ahead=round(d.fs*d.time_fft); % # of samples to grab from impact time to compute fft
nft=2^nextpow2(2*samples_ahead);
d.f_ft=d.fs/2*linspace(0,1,nft/2+1)'; % define frequency vector
window_hold=exp(-4*[1:samples_ahead]'/d.fs); % make exponential window to scale the impact-
induced displacement ring-down data
% exponential window recommended by
Avitable_experimental_modal_analysis_simple_non_mathematical_presentation Sound and Vibration
January 2001

%%
d.tf=[];d.tf_meanoutput=[];d.tf_meansq=[];d.tf_mean=[];data_ft=[];tf_data_on_force=[];data_here=[
];
    for iii=1:d.numlocs
        for jjj=1:d.numhits
            %%
            data_ind=jjj+(iii-1)*d.numhits; % index to retrieve collected data from

            %% filter data
```

```
            ch_f=filtfilt(myfilt,d.data_store(:,data_ind,:)); %

            %%
            temp_ind_1=find(ch_f(d.hitInd(iii,jjj)-
round(d.fs*d.sec_jump):d.hitInd(iii,jjj),1)<0,1,'last')+d.hitInd(iii,jjj)-round(d.fs*d.sec_jump);
% find the start of the impulse peak (voltage crosses 0)

temp_ind_2=find(ch_f(d.hitInd(iii,jjj):d.hitInd(iii,jjj)+round(d.fs*d.sec_jump),1)<0,1,'first')+d
.hitInd(iii,jjj); % find the end of the impulse peak (voltage crosses 0)
            d.force_amplitude(iii,jjj)=max(d.ch_sens(1)*ch_f(:,1)); % find amplitude of force
            d.output_amplitude(iii,jjj,1)=max(d.ch_sens(2)*ch_f(:,2)); % find amplitude of output
            for zzz=1:d.numoutputs
                data_here(:,zzz)=d.ch_sens(zzz+1).*ch_f(temp_ind_1:temp_ind_1+samples_ahead-
1,zzz+1); % current evaluation of force data
% compute decay rate of impulse response from exponential fit of amplitude peaks
atrunc=1:round(.1*length(data_here(:,zzz)));
[holding1,holdind1]=findpeaks(abs(data_here(atrunc,zzz))); % finding peaks from abs data
[holding2,holdind2]=findpeaks(holding1); % refine peaks
temptime=[1:length(data_here(atrunc,zzz))]/d.fs; % create dummy time series
temp_fit=fit(temptime(holdind1(holdind2))',holding2,'exp1');
figure(1);clf;box
on;plot(temptime(holdind1(holdind2))',holding2,'or',temptime(holdind1(holdind2))',temp_fit.a.*exp
(temp_fit.b*temptime(holdind1(holdind2))'),'-b');set(gca,'yscale','log');axis([0 .025 1e-2
100]);drawnow
d.decay_rate(iii,jjj,zzz)=temp_fit.b;

                data_mean_here(zzz)=mean(data_here(:,zzz)); % mean of start/stop data in this
time frame
                data_ft(:,zzz)=fft((data_here(:,zzz)-
data_mean_here(zzz)).*window_hold,nft)/(samples_ahead*mean(window_hold)); % impact fft on disp,
take fast fourier transform of exponentially windowed data
                %data_ft(:,zzz)=fft((data_here(:,zzz)-
data_mean_here(zzz)).*window_hold,nft)/(length(data_here)*mean(window_hold)); % impact fft on
disp, take fast fourier transform of exponentially windowed data

                tf_data_on_force(:,zzz)=data_ft(:,zzz)./d.force_amplitude(iii,jjj);
                d.tf(:,iii,jjj,zzz)=tf_data_on_force(1:nft/2+1,zzz); % impact fft on tf,
magnitude of single-sided fourier transform
            end

            d.tf_meanoutput(:,iii,jjj)=mean(squeeze(d.tf(:,iii,jjj,:)),2); % take mean across
number of simultaneous outputs)

%             figure(23);
%             clf;
%             plot(d.f_ft,abs(d.tf_meanoutput(:,iii,jjj)));
%             xlim([50 2e3]);
%             drawnow

        end
        d.tf_mean(:,iii)=mean(squeeze(d.tf_meanoutput(:,iii,:)),2); % take mean across hits at
location iii
        %     d.tf=[];
    end
    d.tf_meansq=mean(d.tf_mean.^2,2); % take mean across all locations

%%
d.tf_global_mean=(d.tf_meansq).^(1/2); % take mean across locations for global response
d.tf_global_mean_amplitude=2*abs(d.tf_global_mean); % take abs of global mean for plotting
purposes

dolf=erase(d.filename,'.mat');
d.figname1=strcat(dolf,fige1);
d.figname2=strcat(dolf,fige2);

%% plot TF
% figure(8);
% clf;
% % hold on
% loglog(d.f_ft,d.tf_global_mean_amplitude);
% xlabel('frequency [Hz]')
```

```
% ylabel('TF, data/impact force [unit/N]')
% xlim([50 20000])
% title({[d.filename] ['global response of displacement on force'] [num2str(d.numlocs) ' input
locs with ' num2str(d.numhits) ' hits each and ' num2str(d.numoutputs) ' output
locs']},'Interpreter','none')
% figname=d.filename(1:end-4);
% % saveas(gcf,figname,'fig')

%% save data
if saveon==1 && dataacquire==1
    % remove data time series for memory-saving
%     d.time=[];
%     d.data=[];
%     d.time_series=[];
%     d.data_store=[];
    d.tf=[];
    d.tf_meanoutput=[];

    save(d.filename,'d');
end

%%
%% plot octave or one-third octave band measures
ob=1e3*2.^[-6:4]; % octave band center frequencies [Hz]
ob_lo=ob./2.^(1/2); % octave band center frequency lower [Hz]
ob_hi=ob.*2.^(1/2); % octave band center frequency higher [hz]
otob=1e3*2.^([-18:12]/3); % one-third octave band center frequencies [Hz]
otob_lo=otob./2.^(1/6); % one-third octave center frequency lower [Hz]
otob_hi=otob.*2.^(1/6); % one-third octave center frequency lower [Hz]

% determine octave and one-third octave band measures
% octave band
for jjj=1:length(ob)
ind1=max(find(d.f_ft<=ob_lo(jjj)));
ind2=max(find(d.f_ft<=ob_hi(jjj)));
tf_ob(jjj)=(sum(d.tf_global_mean_amplitude(ind1:ind2).^2)).^(1/2);
end
% one-third octave band
for jjj=1:length(otob)
ind1=max(find(d.f_ft<=otob_lo(jjj)));
ind2=max(find(d.f_ft<=otob_hi(jjj)));
tf_otob(jjj)=(sum(d.tf_global_mean_amplitude(ind1:ind2).^2)).^(1/2);
end

colors=['r' 'g' 'b' 'c' 'm' 'k'];
markers=['o' 's' 'd' 'v' '^' '*'];
color_plot=1;

figure(3);
clf;
hold on
box on
% plot(d.f_ft,d.tf_global_mean_amplitude);
plot(d.f_ft,10*log10(d.tf_global_mean_amplitude),'color',colors(color_plot));
xlabel('frequency [Hz]')
ylabel('TF, response/(impact force) [dB re 1 unit/N]')
set(gca,'xscale','log');
% set(gca,'yscale','log');
xlim([50 20000])
title({[strrep(d.filename,'_','-')] ['ratio of global response on force'] [num2str(d.numlocs) '
input locs with ' num2str(d.numhits) ' hits each and ' num2str(d.numoutputs) ' output locs.
height constraint ' num2str(d.constraint_height) ' inch']});
figure(4);
clf;
hold on
box on
% plot(otob,tf_otob,'-o');
plot(otob,10*log10(tf_otob),['-' colors(color_plot) markers(color_plot)]);
xlabel('frequency [Hz]');
ylabel({['1/3-octave band TF'],['response/(impact force) [dB re 1 unit/N]']});
set(gca,'xscale','log');
```

```
% set(gca,'yscale','log');
xlim([50 20000]);
title({[strrep(d.filename,'_','-')] ['ratio of global response on force'] [num2str(d.numlocs) '
input locs with ' num2str(d.numhits) ' hits each and ' num2str(d.numoutputs) ' output locs.
height constraint ' num2str(d.constraint_height) ' inch']});


% compute octave band total measures
% disp([num2str(10*log10(sum(tf_ob(3:end))),'%1.3f') ' [dB] from 62.5 to 16e3 [Hz] octave bands.
' d.filename]);
% disp([num2str(10*log10(sum(tf_ob(3:8))),'%1.3f') ' [dB] from 62.5 to 2e3 [Hz] octave bands. '
d.filename]);
% disp([num2str(10*log10(sum(tf_ob(3:7))),'%1.3f') ' [dB] from 62.5 to 1e3 [Hz] octave bands. '
d.filename]);
d.data_temp_hold(1)=10*log10(sum(tf_ob(4:end))); % store octave band 125 to 16e3 TF
temp_hold_std1=std(tf_ob(4:end));
temp_hold_std=10*log10(temp_hold_std1);
% d.data_temp_hold(2)=10*log10(sum(tf_ob(4:8))); % store octave band 125 to 2e3 TF
% d.data_temp_hold(3)=10*log10(sum(tf_ob(4:7))); % store octave band 125 to 1e3 TF


%% plotting time series data
time_series_set=1;
figure(7);
clf
hold on
plot(d.time_series(:,time_series_set),d.data_store(:,time_series_set,1)*d.ch_sens(1),d.time_serie
s(:,time_series_set),d.data_store(:,time_series_set,2)*d.ch_sens(2));
xlabel('Time (s)');
ylabel('Output [N] or [m/s^2]');
title({[strrep(d.filename,'_','-')] ['time series'] [num2str(d.numlocs) ' input locs with '
num2str(d.numhits) ' hits each and ' num2str(d.numoutputs) ' output locs']});

%%
%%plotting decay rate v force amplitude
figure(984);
clf;
plot(d.force_amplitude,d.decay_rate,'o');
xlabel('force [N]'); xlim([50 450]);
ylabel('decay rate'); ylim([-700 -100]);
title({[strrep(d.filename,'_','-')] ['decay rate v force'] [num2str(d.numlocs) ' input locs with
' num2str(d.numhits) ' hits each and ' num2str(d.numoutputs) ' output locs. height constraint '
num2str(d.constraint_height) ' inch']});
savefig(d.figname1);

%%plotting output amplitude max v force amplitude max
figure(985);
clf;
plot(d.force_amplitude,d.output_amplitude,'o');
xlabel('force [N]'); xlim([50 450]);
ylabel('amplitude of output [m/s^2]'); ylim([2 20]);
%title({[strrep(d.filename,'_','-')] ['decay rate v force'] [num2str(d.numlocs) ' input locs with
' num2str(d.numhits) ' hits each and ' num2str(d.numoutputs) ' output locs']});
title({[strrep(d.filename,'_','-')] ['output amplitude v force'] [num2str(d.numlocs) ' input locs
with ' num2str(d.numhits) ' hits each and ' num2str(d.numoutputs) ' output locs. height
constraint ' num2str(d.constraint_height) ' inch']});
savefig(d.figname2)
```